NTNU
Norwegian University of
Science and Technology

CO2 Sequestration - a Near-Well Study

Espen Høegh Sørum

Master of Science in Physics and Mathematics
Submission date: June 2017
Supervisor: Xavier Raynaud, IMF
Co-supervisor: Odd Asbjørn Andersen, SINTEF IKT

Norwegian University of Science and Technology
Department of Mathematical Sciences

Abstract

Carbon Capture and Storage (CCS) has been proposed as a promising and necessary tool in strategies for mitigating the effects of anthropogenic climate change. Deep geological formations, like saline aquifers, are pointed out as promising areas for large-scale storage of CO_2. To address questions relating to storage capacity and safety issues various computational models have been developed. A particularly useful modelling framework is the vertical-equilibrium (VE) model, which is based on the assumption of negligible vertical flow . Such a model is preferred when studying large-scale and long-term migration of CO_2 in aquifers due to their computational efficiency.

However, the VE assumption leads to inaccurate solutions close to injecting wells, in so-called near-well areas. As the underlying VE assumption does not hold in these regions, flow here has to be modelled using a conventional 3D multi-phase approach, which poses a significantly higher computational demand. In order to bridge the gap between the VE and 3D modelling domains, a hybrid model has recently been proposed. In the hybrid model, the interface between the two domains is defined by a separation radius around injection wells. However, the optimal choice of this radius remains an open question. In the present work, the choice of radius is investigated using both a numerical and an analytical approach.

Using `MRST`, a free open-source simulation tool kit for reservoir modelling and simulation developed at SINTEF Digital, this thesis studies the conditions under which VE can be assumed in the near-well area and calculates the separation radius numerically. The separation radius can also be determined using an analytical solution for the height of the CO_2 plume in a special injection scenario. Simulations with hybrid models are also conducted and compared to simulations from pure VE and 3D models.

Simulations herein indicates that the VE assumption is not valid for geological formations with low permeability (10 milliDarcy) and cubic relative permeability curves, as this leads to long drainage time of brine from the CO_2 plume. Results for both the numerical and analytical separation radius show that after a certain injection time VE can be assumed in the whole aquifer, i.e. the separation radius is zero. The numerical and analytical results show also some clear differences, despite efforts to ensure as small theoretical differences as possible.

The analytical solution tends to under-predict the region with negligible vertical flow compared with the numerical solution, whereas an overprediction would be more desirable from a practical point of view. Hence more research is needed before the analytical approach can be used for predicting the separation radius. Simulations with the hybrid model illustrates that they can significantly reduce computational requirements compared to a full 3D model, while preserving the accuracy of a full 3D solution close to the well in short-term simulations. More research and long-term simulations have to be conducted before any conclusions can be drawn of benefits and disadvantages of a hybrid model versus a pure VE model, which still is the preferred model for long-term simulations.

Sammendrag

Karbonfangst og -lagring har blitt foreslått som et lovende og nødvendig verktøy i strategier for å redusere effektene av menneskeskapte klimaendringer. Dype, geologiske formasjoner, som akviferer, er utpekt som lovende områder for storskala lagring av CO_2. For å besvare spørsmål relatert til lagringskapasitet og sikkerhet, har ulike beregningsmodeller blitt utviklet. Et spesielt nyttig modelleringsramme er vertikal likevektsmodellen (VL), som er basert på antagelsen om ubetydelig vertikal flyt. En slik modell er foretrukket for storskala- og langtidsstudier av migrasjon av CO_2 i akviferer grunnet dens beregningsmessige effektivitet.

VL-antakelsen fører imidlertid til unøyaktige løsninger nær injeksjonsbrønner, i såkalte nærbrønnområder. Den underliggende VL-antagelsen er ikke gyldig i disse områdene, og flyten må her modelleres ved bruk av en konvensjonell 3D-tilnærming, noe som medfører et betydelig høyere krav til datakraft. For å kunne knytte domene til en VL- og 3D-modell sammen, har en hybrid modell nylig blitt foreslått. I hybridmodellen er grensesnittet mellom de to domenene definert av en separasjonsradius rundt injeksjonsbrønner. Det optimale valget av denne radiusen er imidlertid et ubesvart spørsmål. Denne oppgaven undersøker valget av radius med en numerisk og en analytisk tilnærming.

Ved bruk av `MRST`, et fritt tilgjengelig simuleringsverktøy for reservoarmodellering og - simulering utviklet hos SINTEF Digital, undersøker denne oppgaven vilkårene for VL - antagelsen i nærbrønnområdet og beregner separasjonsradiusen numerisk. Separasjonsradiusen kan også bestemmes ved hjelp av en analytisk løsning for høyden av CO_2-fasen i et spesifikt injeksjonsscenario. Simuleringer med hybridmodeller er også utført og sammenlignet med simuleringer fra rene VL- og 3D-modeller.

Simuleringer gjort indikerer at VL-antakelsen ikke er gyldig for geologiske formasjoner med lav permeabilitet (10 milliDarcy) og kubiske relativ permeabilitetskurver, da dette fører til lang dreneringstid av vann ut av CO_2-fasen. Resultatene for både den numeriske og analytiske separasjonsradius viser at etter en viss injeksjonstid kan VL antas i hele akviferen, noe som tilsvarer at separasjonsradien er null. De numeriske og analytiske resultatene viser også noen klare forskjeller, til tross for forsøk for å sikre så små teoretiske forskjeller mellom fremgangsmåtene.

Den analytiske løsningen tenderer til å underestimere regionen med ubetydelig vertikal flyt i forhold til den numeriske løsningen, mens en overestimering er mer ønskelig fra et praktisk synspunkt. Derfor er det

behov for mer forskning før analytisk tilnærming kan brukes til å forutsi separasjonsradien. Simuleringer med hybridmodellen illustrerer at den kan redusere beregningstiden betydelig sammenlignet med en ren 3D-modell, samtidig som nøyaktigheten av en ren 3D-løsning nær brønnen er beholdt i korttids-simuleringer. Mer forskning og langtids simuleringer må gjennomføres før det kan konklusjoner kan sluttes angående fordeler og ulemper ved en hybridmodell versus en ren VL-modell, som er den foretrukne modellen for langtids simuleringer.

Preface

This master thesis completes my studies at the Norwegian University of Science and Technology (NTNU) in the field of applied mathematics. The work was carried out during the spring semester of 2017 at the Deparment of Mathematical Science in Trondheim, Norway in cooperation with SINTEF Digital in Oslo, Norway. The idea of the project was brought up by my co-supervisor at SINTEF Digital, Odd Andersen, as a contribution to their ongoing work with modelling of CO_2 sequestration.

It is assumed that the readers of this report have some background in science or academia. Even though the thesis is under the field of applied mathematics a very deep knowledge of mathematics is not necessary, but a background in engineering, mathematics or physics is beneficial.

My sincere gratitude and thanks goes to my co-supervisor, Odd Andersen, for sharing his knowledge with me and guiding and support in this project. His contribution to this thesis has been invaluable. I would also like to thank my supervisor Xavier Raynaud for taking care of all the formalities and employee at SINTEF Digital Olav Møyner for his contribution to the hybrid model.

I would also like to send my gratitudes to my friends here in Trondheim, whom have made the last five years some of the most memorable and fun years of my life.

Trondheim, 18.06.17
Espen Høegh Sørum

Contents

Chapter 1

Introduction

1.1 Background

CO_2 concentration in the atmosphere is naturally dynamic, but over the last century the concentration has increased significantly. Figure 1.1 shows how the concentration has increased since the industrial revolution and also sets today's concentration in a historic perspective. The dashed lines at 300 and 170 ppm (parts per million) indicates the maximum and minimum values of atmospheric CO_2 concentration in ice cores for the past 650,000 years before the industrial age. The current value measured at the Mauna Lao Observatory situated in Hawaii is at around 400 ppm[1], which sets today's level of CO_2 at a historic high level. In recent years the emissions of CO_2 have emerged as one of the greatest global challenges, as CO_2 is widely acknowledged as the primary contributor to anthropogenic climate change [1]. The impacts of climate change are widespread, and to mention some are impacts on the hydrological cycle, notably the availability of freshwater resources, permafrost warming, significant change in the physical and chemical properties of oceans and a rise in global temperature [1]. At the Paris climate conference in December 2015, 195 countries adopted the first-ever universal, legally bounding climate deal. The key element of The Paris Agreement is to strengthen the global response to the threat of climate change by keeping a long-term global temperature rise below 2°C above pre-industrial levels [2, 3].

[1] Daily CO_2 levels at the Mauna Lao Observatory can be accessed at https://www.co2.earth/daily-co2

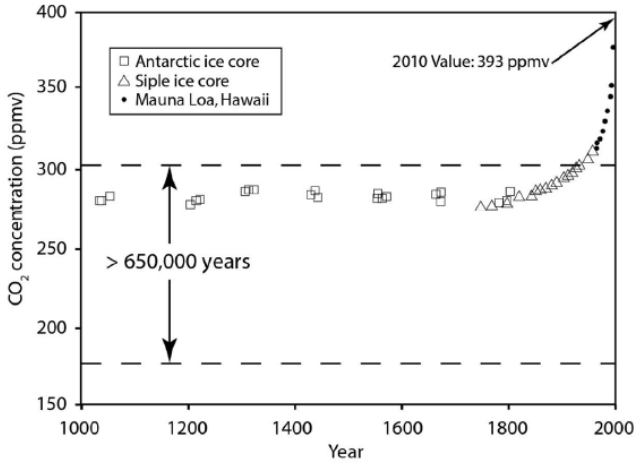

Figure 1.1: Atmospheric CO_2 concentration over the past 1000 years. The dashed lines shows the range CO_2-concentrations measured over the past 650,000 years before the industrial age. The figure is taken from [4] with approval.

1.1.1 Carbon Capture and Storage

As a possible large-scale mitigation strategy for the atmospheric carbon problem, Carbon Capture and Storage (CCS) has emerged as a serious option for offsetting a fraction of the global atmospheric emissions. The goal is that CCS can function as a temporary bridge between a fossil fuel-based economy and a future economy based on renewable energy. Most future scenarios that meet the 2-degree goal rely on widespread use of CCS, while the absence of which would more than double the cost of reaching the target [5]. The Intergovernmental Panel on Climate Changes' (IPCC) special report on CCS [6] provides many details about the overall concept and technical approaches for possible implementation. The report concludes the the overall global storage capacity of CO_2 appears to be more than adequate in order to have an actual impact on global CO_2 levels.

The concept of CCS is quite straightforward, and Figure 1.2 illustrates the principles of CCS. First, CO_2 that otherwise would have been emitted into the atmosphere is captured, e.g. from production of electrical energy or industrial production. The captured carbon is then sequestered somewhere else than in the atmosphere. The most likely location for large-scale sequestration is in deep geological formations. Figure 1.3

shows promising areas for CO_2 storage across the globe. Here large areas of saline aquifers are identified as possible storage sites. The rock of a geologic formation (such as an aquifer) is characterized by its permeability and its porosity. Permeability is a measure of the ability of the aquifer to allow fluids to pass through it, i.e. the permeability within the aquifer has to be large enough such that CO_2 flows in the aquifer, but the aquifer must also be confined by formations with low permeability such that CO_2 does not leak. The porosity is the pore space of the aquifer available for fluids to flow in, i.e. the void space in the sandstone. The higher the porosity is, the higher is the storage capacity of the aquifer. A saline aquifer may meet three requirements for a promising storage cite; (i) it is sufficiently permeable to accept large quantities of CO_2, (ii) it is confined on top and below by some formations of very low permeability that will keep the injected buoyant CO_2 in place and (iii) the porosity of the aquifer is sufficiently large to store a considerable amount of CO_2.

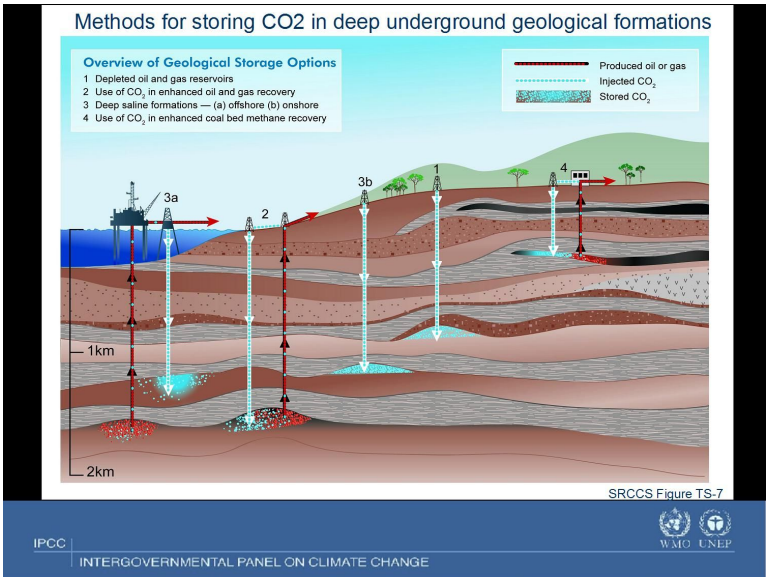

Figure 1.2: Illustration of CCS. The figure is taken from [6] with approval.

Even though the technology for large scale CCS deployment exists and CCS seems like a very promising contribution for mitigating atmospheric carbon concentration, there are challenges that have to be solved before CCS can have a significant effect on global carbon concentration. According to the Global CCS Institute there are currently only 21 large-

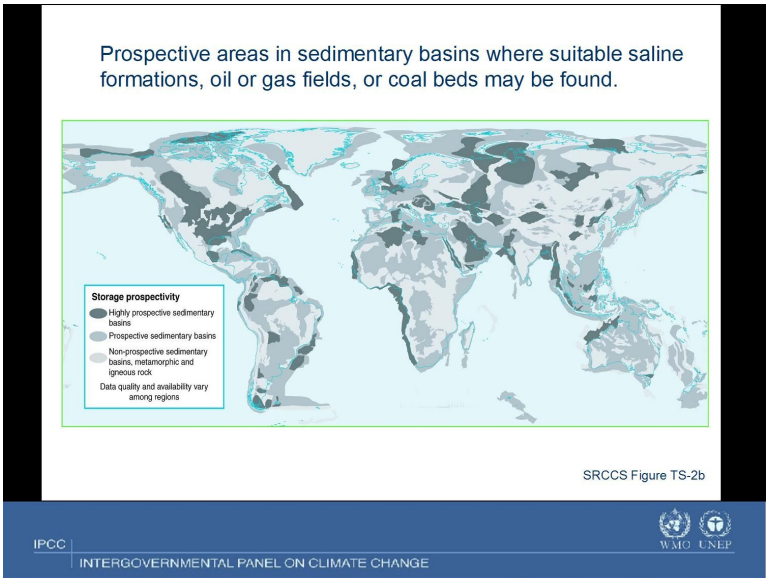

Figure 1.3: Prospective areas for geological storage of CO_2. The figure taken from [6] with approval.

scale CCS projects in operation or under construction globally [2]. Furthermore, the experience with the long-term effects of deep geological storage of CO_2 is minimal. The Norwegian Shøhvit Project [7] was the first pure CO_2 storage project when it started up in 1996. However, this project has been ongoing for just over 20 years, which is very short compared to the potential storage time of thousands of years. In addition, if CCS is to have a significant impact on the global concentration of CO_2, today's injection rates, which rarely exceed 1 Mt (megatonne) per year, have to be substantially increased, and global storage operations must be scaled up by orders of magnitude.

Therefore, the upscaling from today's projects raise questions that have to be answered. These questions can in general be divided into three parts

1. **Storage capacity.** How much CO_2 can a formation store?

2. **Injectivity.** How efficiently can CO_2 be injected into a formation?

3. **Containment.** How sure can one be that the CO_2 will remain in a

[2] The GLobal CCS Institute online Projects Database can be accessed at www.globalccsinstitute.com/projects/large-scale-ccs-projects.

formation?

In order to answer these questions at the operational scales considered, numerical simulations constitute an indispensable tool.

1.1.2 MATLAB Reservoir Simulation Toolbox

The MATLAB Reservoir Simulation Toolbox (MRST) [8, 9], developed by The Computational Geosciences group within the Department of Scientific Computing at SINTEF Digital, is an open-source software tool kit whose functionality can be used for modelling flow both in petroleum production and CO_2 sequestration in reservoirs. One add-on module of MRST is MRST-co2lab, which consists of a family of tools specially developed for the study of long-term storage of CO_2 in large-scale aquifer systems [10].

The main focus of MRST-co2lab is simplified models particularly suited for studying long-time developments. One model is based on a depth-integrated physical description of formations with the additional assumption of vertical equilibrium (VE) between CO_2 and brine. The depth-integrated model reduces the number of spatial dimensions from 3 to 2, which allows for simulations that run orders of magnitude faster than traditional 3D simulations. This makes it computationally tractable to simulate large-scale, long-term scenarios, which is needed when studying long-term CO_2 migration. VE models are based on the fact that in typical aquifer formations the vertical extent is measured in tens of meters, while the extension of the CO_2 plume is in the order of kilometres during the injection phase and possibly much greater in a migration phase, meaning that that the vertical flow will constitute very little to the overall flow. Moreover, there is a significant difference between brine and CO_2 (whether in supercritical or liquid state) density in practically all relevant scenarios. This difference means that brine and CO_2 will tend to segregate relatively quickly due to gravity forces. The separation process can be considered complete when vertical equilibrium has been established between capillary and gravity forces. The flow is usually confined to thin layers underneath a sealing caprock or other low-permeability layers. This yields a large disparity in lateral and vertical scales. In order to avoid introducing large errors in the forecast of the up-dip migration in 3D simulations, the vertical fluid distribution must therefore be represented accurately. In practice, this means using a higher vertical grid resolution than what is computationally tractable in standard

3D simulators, and as a result, 3D simulations tend to be severely under-resolved unless they are conducted using large-scale systems for high-performance computing.

In a VE model, the primary assumption is that the flow system is in vertical equilibrium so that the vertical distribution of fluid phases can be determined from analytical expressions. By integrating the flow equations in the vertical direction a 2D model is obtained. See Figure 1.4 for an illustration of a 3D and VE grid. From this figure is should be clear why VE model is sometimes referred to as an *upscaled system*, while a 3D model is referred to as a *fine-scale system*. Integration in the vertical direction not only reduces the number of spatial dimensions, and hence the required number of grid cells, but will also lessen the coupling between pressure and fluid transport and improves the characteristic time constants of the problem. As a results, vertical-equilibrium simulations will typically be orders of magnitude faster and consume significantly less memory than conventional 3D simulators.

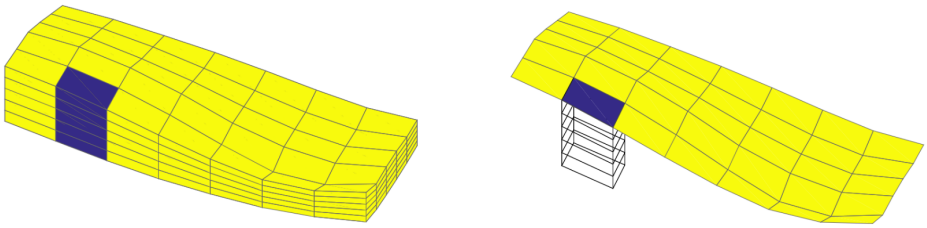

Figure 1.4: Illustration of the same grid in a 3D (left) and VE (right) simulation. The wire frame cells on the right plot are not part of the 2D grid itself, but used to illustrate that the blue 2D cell is used to represent the full stack of yellow cells in the 3D grid on the left. The figure is taken with approval from [14].

When considering the long-term migration of a well-formed CO_2 plume, the error introduced by using a VE simulator may be significantly smaller than a coarse 3D simulator. However, when considering the injection phase VE models may not perform better than 3D models. As stated in [11] there is significant vertical flow in the vicinity of injecting or extracting wells. In such near-well areas the VE assumption does not hold.

Over the last decade, significant research effort has been put into developing VE models to a high degree of sophistication. Worth to mention are the Vertical Equilibrium with Sub-scale Analytical (VESA) method [12], which combines a large-scale numerical method with embedded

analytical solutions to capture sub-scale flow through leaky wells, and a multi-scale multilayer vertically integrated model [13], which relaxes the VE assumption by including two-phase flow dynamics of brine and CO_2 as a fine-scale one-dimensional problem.

Another approach used in this thesis is to create a combined VE and 3D model, a so-called hybrid model that captures the benefits of both models. The goal of a hybrid model is to handle large-scale scenarios, i.e. scenarios that are so large that a 3D model is not practically applicable everywhere, but where the precision of a full 3D model near the injection or extraction wells is still desired. An example is a scenario that models wells extracting brine to ease the pressure in the aquifer. In such a scenario the flow around the well has to be modelled with a high precision, to ascertain that brine and not CO_2 is extracted. A hybrid model could therefore use a full, numerical 3D simulation in the vicinity of wells, and couple this with a VE model in areas with non-significant vertical flow. This is a relatively recent development, which will likely lead to further research in the near future.

In order to create a valid hybrid model, regions with significant vertical flow have to be identified. In such a hybrid model there is an interface between the 3D domain and the VE domain. Around a vertical well it is natural to think that this interface is placed at a radius R^* around the well, where there is significant vertical flow in the area within this radius.

1.2 Objectives

The objectives of this master thesis can be divided into three parts. Firstly, this thesis aims to compare VE and 3D simulations using `MRST` during the injection phase of CO_2 and examine under which conditions the VE assumption holds. The second objective is to determine analytically and numerically where the boundary between the VE and 3D domain in a hybrid model should lie, and compare results from the approaches. Finally, this report concentrates on simulations with a hybrid model, and compares results from hybrid simulations with full VE and 3D simulations.

1.3 Structure of the Report

In this introductory chapter the reader has been familiarized with Carbon Capture and Storage, ways to model storage of CO_2 in aquifers and some of the challenges within this modelling. Following the current chapter is a theoretical chapter that covers a physical description of CO_2 and brine flow in an aquifer, specifications of a 3D, VE and hybrid model and a numerical and analytical approach for determining the VE and 3D domain in a hybrid model. After this follows a chapter with numerical results and discussions for the three objectives of the thesis, before the final chapter concludes and remarks further work.

Chapter 2

Theory

This chapter is divided into three parts. First, a description of two-phase flow in an aquifer is given. This description starts off describing physical properties of fluids and the geological formation, and ends with presenting the governing equations that determine the two-phase flow. Following the description of the two-phase flow system are three approaches for solving the governing equations. These methods are the full, 3D finite-volume method, the fast vertical equilibrium (VE) method and a combination of the two methods, which is referred to as the hybrid method. The last theoretical section covers methods for dividing the computational grid into a 3D and VE part, by finding a separation radius R^* around an injecting well.

2.1 Two-Phase Flow in porous Medium

This section describes the porous medium system, highlights the dominant chemical and physical processes and develops the governing equations that determine the two-phase flow. The contents is based on [4, 14, 15], and a more thorough description can be found in any of these references.

2.1.1 Qualitative Description

The flow of multiple phases in a porous medium is extremely complex. Hence, this part will only cover the most basic concepts of the two-phase flow of CO_2 and brine in a porous medium relevant for this master project. The term *phase* is here used to denote a substance (either CO_2 or brine),

independent of its state (solid, liquid, gas, supercritical). When CO_2 is injected into an aquifer, it has to be injected at a sufficiently high pressure, such that the initial brine in the pore spaces is displaced. This pressure is referred to as the *entry pressure*, and the process of injecting CO_2 creates fluid-fluid interfaces at the pore scale that allow the two fluids to coexist in the pore spaces. These interfaces play an important role in determining the two-phase flow, as they can support non-zero stresses, which allow the two fluids to coexist at different pressures, and because mass transfer between CO_2 and brine occurs at these interfaces.

As brine is more dense than CO_2, the two fluids will relative quickly separate such that CO_2 flows at the top of the aquifer and brine at the bottom, as illustrated in Figure 2.1. In this thesis it is assumed that there is a *sharp interface* between the brine and CO_2, while there in reality exists a transition zone caused by the presence of capillary pressure. This zone is referred to as the capillary fringe, and represents a smooth transition from CO_2 to the brine below. It has been shown that even a modest capillary fringe has a first-order impact on the formation of plumes both near an injection point and on migration [16], and therefore one should be careful about using results derived under the assumption of sharp interfaces for quantitative assessment in the presence of significant capillary pressure.

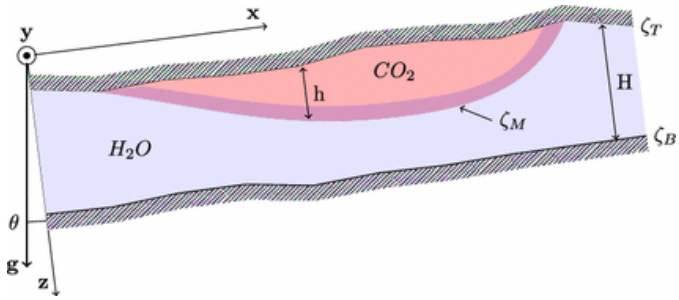

Figure 2.1: Illustration of how a CO_2 plume flows in an aquifer. ζ_T and ζ_B represent the shape of the caprock and bottom confining layer, while ζ_M describes the shape of the brine-CO_2 interface. H and h denote the local height of the aquifer and the CO_2 plume, while θ is the angle between the z coordinate axis and the gravity vector $\boldsymbol{g}$. The different colors of the CO_2 plume represent the transition zone between CO_2 and brine. The figure is taken from [18] with approval.

As the CO_2 and brine face are in contact with each other, some amounts

of CO_2 is dissolved into the brine. This effect is most important during the migration stage, as the large spatial extent and flattening of the CO_2 increases the amounts of brine and CO_2 in contact with each other [17]. As CO_2-saturated brine is slightly denser than unsaturated brine, the heavier saturated brine sinks downwards. Dissolved CO_2 thus becomes safely stored at the bottom of the aquifer with no no risk of leaking through cracks in the caprock. This is referred to as *dissolution trapping*. As this thesis only considers the injection period, it is in the following assumed that no mass transfer between CO_2 and brine occurs.

Dissolution trapping is one of four major trapping mechanisms in the context of geological storage of CO_2. The remaining three are *residual, structural* and *mineral* trapping. Residual trapping refers to the CO_2 trapped within the brine phase as brine reinvades pore space that CO_2 evacuates. Structural trapping refers to CO_2 that is permanently trapped within local pockets, anticlines or other topographical features that the injected CO_2 passes. The final trapping mechanisms, mineral trapping, refers to geochemical reactions where dissolved CO_2 precipitates as carbonate materials, which is dependent on the chemical composition of the pore water and rock as well as temperature and pressure.

Figure 2.2 shows a porous medium with two fluids on the pore scale. The solid phase (rock) will tend to have a stronger surface attraction to one of the fluids, and this fluid is referred to as a the *wetting phase*. For the CO_2-brine system this will be brine, and CO_2 is therefore referred to as the *non-wetting phase*. Brine and CO_2 combined occupy a fraction of the total space, and this fraction is referred to as the *porosity* ϕ. In order to describe the system one also needs to define the fraction of pore space occupied by each of the fluids. The *fluid saturation* s_α is defined as the fraction of pore space occupied by fluid phase α. Here α denotes either the wetting phase ($\alpha = w$) or the non-wetting phase ($\alpha = n$). Since brine and CO_2 are the only two fluids present, the sum of the saturations is equal 1, i.e. $s_w + s_n = 1$. Note that the interfaces that exist on the pore scale given in Figure 2.2 play an important role in understanding the behaviour of the two-phase system, but in modelling one is interested in describing the system on larger scale. The pore-scale phenomena is thus represented by upscaled quantities at the macroscale, such as porosity, permeability, and capillary pressure curves.

In addition to phase saturations, each phase is also associated with a *volumetric flux vector*, $\boldsymbol{u}_\alpha$. Here and throughout this thesis bold symbols describe vector parameters. $\boldsymbol{u}_\alpha$ is a measure of the volumetric flow rate

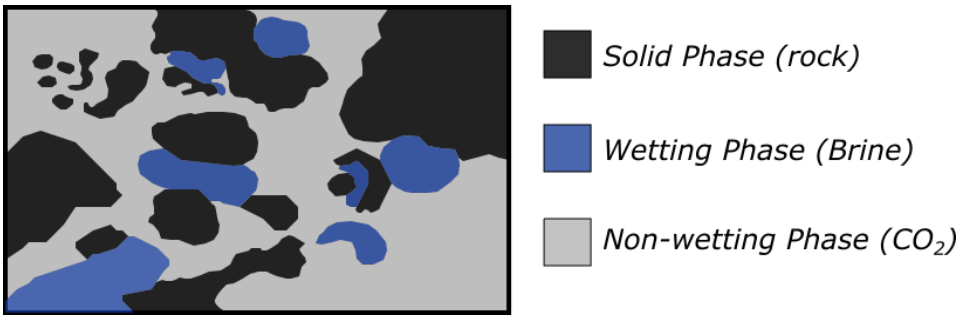

Figure 2.2: Fluid and solid distributions in a porous medium on the pore scale. With approval, this figure is inspired by a similar figure that can be found in [4].

per area of the porous medium. This is not a direct measure of flow velocity, but can be seen as the volume of fluid per total area (which includes both fluid and solid) per time. The actual fluid velocity $\boldsymbol{v}_\alpha$ is a scaled version of the flux vector $\boldsymbol{u}_\alpha$, where the scale factor is the the fraction of total space occupied by the fluid. This gives $\boldsymbol{v}_\alpha = \boldsymbol{u}_\alpha / \phi s_\alpha$. Further, each phase has its own pressure, denoted by p_α. As mentioned, the fluid-fluid interface can support non-zero stresses, which signifies that different pressures can exist on either side of the interface. In general, the phases will thereby have different pressures, and the difference between the phase pressures is defined as the *capillary pressure* p_{cap}.

$$p_{cap} \equiv p_n - p_w \tag{2.1}$$

Two more fluid properties that are important when simulating fluid flow are *density* ρ_α and *dynamic viscosity* μ_α. Density is important as it relates volumes with fluid mass, and viscosity is important as it measures a fluids resistance to shear deformation, and thus its resistance to flow through a porous medium. Density is a thermodynamic property, meaning that it is related to other thermodynamic properties as pressure and temperate by an *equation of state*. Viscosity is a *transport property*, but there exists empirical fluid-specific correlations that associate it with thermodynamic properties. Under the assumption of a *isothermal* model, density and viscosity can be modelled as functions of pressure. A simpler model also assumes constant *compressibility* c_f. Compressibility for

a fluid is given as

$$c_f = \frac{1}{\rho}\frac{d\rho}{dp}$$

Assuming that the compressibility is constant over some pressure range, density can be written as a function of pressure if a reference density ρ_0 is known at some reference pressure p_0

$$\rho(p) = \rho_0 e^{c_f(p-p_o)}$$

The same relationship is often used to model changes in pore volumes as a function of pressure, by defining the *pore volume compressibility* as $c_\phi = \frac{1}{\phi}\frac{d\phi}{dp}$. The same relation is used since an increase in fluid pressure expands the rock matrix and increases the volume available for the fluids.

2.1.2 Darcy's Law for two-phase Flow, Relative Permeability and Residual Saturation

In 1856 Henry Darcy performed experiments that provided one of the fundamental equations for groundwater *single-phase* flow [15]. The fluid velocity $\boldsymbol{v}$ was found to be linearly dependent with the pressure gradient ∇p in the following form

$$\boldsymbol{v} = -\frac{\boldsymbol{K}}{\mu}(\nabla p - \rho \boldsymbol{g})$$

Here $\boldsymbol{K}$ is the permeability tensor and $\boldsymbol{g}$ is the gravity vector. As mentioned this relation is valid for single-phase flow. However, by introducing *relative permeabilities* Darcy's equation can still be used indirectly for two-phase flow. The permeability coefficient in Darcy's equation is an intrinsic property of porous materials and governs the ease in which fluids can flow through the pore space. If one consider the flow of for instance the non-wetting fluid in a porous medium containing both the wetting and non-wetting fluid, then the amount of pore space available to the non-wetting fluid is only a fraction of the pore space. Compared to single-phase flow, the space available for flow is reduced, and it is expected that the permeability decreases as fewer flow channels are available for the non-wetting fluid. More precisely, the permeability will decrease as the saturation of the non-wetting fluid decreases, eventually reaching zero when there are no longer any connected pathways of the

non-wetting fluid through the pore space of the medium. The reduction is also linked to effects arising from phase-phase and phase-rock interactions at the molecular level, such as surface tensions and wettability.

The relative permeability $k_{r,\alpha}$ of a phase can be defined as the ratio of fluxes as a function of saturation

$$k_{r,\alpha}(s_\alpha) = \frac{f_\alpha(s_\alpha)}{f_\alpha^{sat}}$$

Here α again denotes the fluid, and f_α^{sat} denotes the flux at fully saturated conditions, that is, $s_\alpha = 1$. There exists a great number of k_r-s (relative permeability-saturation) relationships available in the literature, some are made from fitting experimental data and others are purely mathematical relationships [19]. Figure 2.3 show an experimental relative permeability curve, and two important features can be seen in this figure.

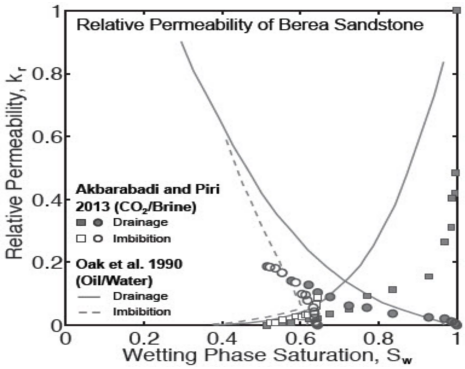

Figure 2.3: Drainage-Imbibition relative permeability curves of Berea Sandstone for the CO_2-brine and a oil-water system (taken from [19] with approval).

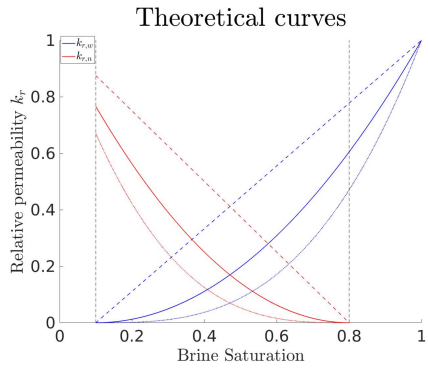

Figure 2.4: Theoretical relative permeability curves. Dashed, solid and dotted line represent respectively a linear, quadratic and cubic k_r-s relationships.

Firstly, there is one curve for drainage and one curve for imbibition. Drainage or imbibition refers to the action where CO_2 displaces or is being displaced by brine, respectively. Therefore the relative permeability curve for the phases exhibits *hysteresis*, i.e. there are different curves depending on whether the wetting saturation is increasing or decreasing. In this thesis hysteresis is not being considered, giving that the same relative permeability curve describes flow for both drainage and imbibition. Note also that since this thesis consider the injection phase, the

occurrence of imbibition is limited. The second feature is that the relative permeability curve reaches zero before brine saturation is zero. As CO_2 is injected into an aquifer it replaces the brine that originally was there, but some brine will be stuck in the pore space as disjoints droplets and films due to capillary forces. This is referred to as *residual brine*, and its fractional amount of the pore space is named *residual brine saturation* $s_{w,r}$. This means firstly that even though some brine is present in a pore space it does not form a continuous pathway and is thus no longer able to flow. Secondly it means that CO_2 will never reach a higher saturation level than $1 - s_{w,r}$. A similar phenomenon occurs when brine invades a pore space originally filled with only CO_2, as some of the CO_2 will remain in the pore space. This amount of CO_2 is referred to as *residual* CO_2, and its saturation value is denoted $s_{n,r}$. Figure 2.4 shows theoretical relative permeability for brine (blue) and CO_2 (red) with residual saturations $s_{r,w} = 0.1$ and $s_{r,n} = 0.2$. Note that the curve for CO_2 is cut off at $s_w = s_{r,w}$, which corresponds to $s_n = 1 - s_{r,w}$, as the CO_2 saturation never will exceed this level. For simplicity this thesis only conducts simulations where residual saturation is set to be zero for both phases. The extension to models and simulations that includes residual saturation is relatively straightforward.

Finally, the two-phase formulation of Darcy's law is given as

$$\boldsymbol{v}_\alpha = -\boldsymbol{K}\lambda_\alpha(\nabla p_\alpha - \rho_\alpha \boldsymbol{g}), \qquad \alpha = w, n \tag{2.2}$$

Here $\boldsymbol{K}$ is the absolute permeability tensor and $\lambda_\alpha = k_{r,\alpha}/\mu_\alpha$ is the *mobility* of phase α.

2.1.3 Capillary Pressure

As stated in (2.1), there is a difference in brine and CO_2 pressure known as the capillary pressure. When a porous medium contains pores with a distribution of different sizes, it is possible to express capillary pressure as a function of phase saturation, i.e. $p_{cap} = p_{cap}(s_w)$. For a particular fluid-rock system, this relationship can be experimentally measured. To understand this relationship physically, one need to examine the two-fluid system on the pore scale. On this scale, the distinct fluid-fluid interfaces serve as boundaries between the fluid phases [15]. Interfaces between the brine and CO_2 phases exist because of small-scale attractive forces between the fluid phases, and these forces result in an interface

that is similar to a membrane, wherein the interface can support a certain amount of stress without rupturing. Such a stress is generated across fluid-fluid interfaces whenever the fluids on either size of the interface have different pressures.

A typical $p_c - s$ (capillary pressure-saturation) relationship is presented in Figure 2.5. Four important features of these curves can be observed. Firstly, in order to see any significant changes in brine saturation when CO_2 displaces brine (see main and primary drainage curves), a non-zero capillary pressure must be applied. This is in fact what was earlier referred to as the *entry pressure*. The second observation is that brine saturation does not go to zero when the capillary pressure p_{cap} goes to infinity, but approaches an asymptotic value greater than zero. This is due to residual brine saturation $s_{r,w}$. Similarly, when brine displaces the CO_2 (imbibition), CO_2 saturation does not return to zero when $p_{cap} = 0$, but remains at the residual non-wetting fluid saturation $s_{r,n}$. The third observation is that the paths followed during drainage and imbibition are different, meaning that the p_c-s relationship, just like the k_r-s relationship, exhibits hysteresis. Finally, the last observation is that *scanning curves* describe the the p_c-s relationship for curves between the two fluids residual saturation.

The important point that has been made is that there exists some relationship between capillary pressure and brine saturation, and this relationship may be quite complex. For the purposes of this thesis, only models with a sharp interface between CO_2 and brine zones are considered. This is equivalent to assuming a capillary pressure equal zero.

2.1.4 Governing Equations

The governing equations for the flow in the porous medium system is determined by the general conservation law, which is given as

$$\int_\Omega \frac{\partial m}{\partial t} dV + \oint_{\partial\Omega} \boldsymbol{f} \cdot \boldsymbol{n} dA = \int_\Omega \psi dV$$

Here Ω and $\partial\Omega$ is the domain and boundary of the domain, respectively, m is mass per total volume of porous medium, $\boldsymbol{f}$ is the mass flux vector, $\boldsymbol{n}$ is the outward-pointing unit vector normal to the surface $\partial\Omega$ and ψ represents sources and sinks within the domain, given as mass per volume per time. Applying the Divergence Theorem on the boundary integral

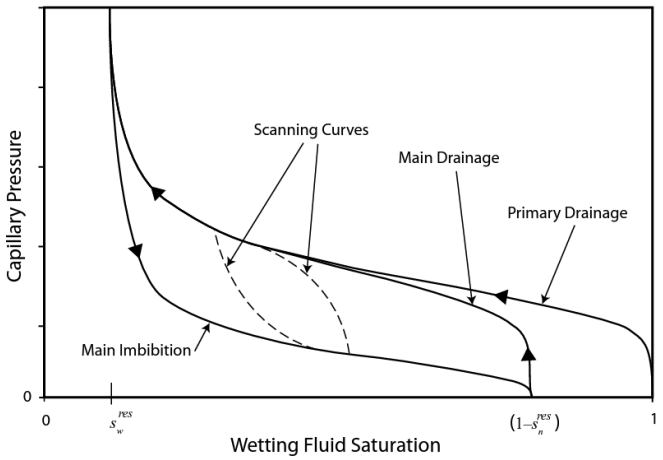

Figure 2.5: Typical form of capillary pressure-saturation curve. The figure is taken from [4] with approval.

yields the following equation

$$\int_\Omega \left(\frac{\partial m}{\partial t} + \nabla \cdot \boldsymbol{f}\right) dV = \int_\Omega \psi \, dV$$

Since the domain Ω was taken to be some arbitrary domain the integrands have to equalize, which gives the following the partial differential equation

$$\frac{\partial m}{\partial t} + \nabla \cdot \boldsymbol{f} = \psi$$

In general, the flow is *miscible*, meaning that brine and CO_2 may consists of multiple components. For instance some CO_2 may dissolve into the brine phase, giving that some CO_2 contributes to the total brine mass. With miscible flow the flux term $\boldsymbol{f}$ will constitute of a dispersive and a diffusive term. The dispersive term is given using the two-phase extension of Darcy's law (2.2) and the diffusive term can be determined using e.g. Fick's law. The work of this thesis is limited to the case of *immiscible* flow, giving that the CO_2 and brine phase is completely separated at all times and no dissolution or evaporation of one phase into the other occurs. Thus the flux term is given as $\boldsymbol{f}_\alpha = \rho_\alpha \boldsymbol{v}_\alpha$. Then mass conservation of each phase α is given as

$$\frac{\partial (s_\alpha \rho_\alpha \phi)}{\partial t} + \nabla \cdot \left(\rho_\alpha - \frac{K k_{r,\alpha}}{\mu_\alpha}(\nabla p_\alpha - \rho_\alpha \boldsymbol{g})\right) = \psi_\alpha, \qquad \alpha = w, n \tag{2.3}$$

There are four variables in the equation above, s_w, s_n, p_w and p_n, meaning that two more equations are needed to match the number of unknowns. These two equations, hereunder referred to as the *supplementary equations* are given by the requirement for the phase saturations to sum up to one and the p_c-s relationship

$$\begin{aligned} s_w + s_n &= 1 \\ p_n(s_n) - p_w(s_w) &= p_{cap}(s_w) \end{aligned} \tag{2.4}$$

One saturation and one pressure unknown can be eliminated from (2.3) using these relations, resulting in a equation system with one phase pressure and one phase saturation as primary variables.

2.2 Solving the two-phase Flow System

This section focuses on how to solve the governing equations given in (2.3) and (2.4). First, the most standard method is presented, namely solving them using a 3D cubic grid. Secondly the fast VE method is introduced, before the combination of the 3D and VE method, the hybrid method, is presented.

2.2.1 3D Model

The equations determining the reservoir flow are continuous, but when solved with a numerical simulator they are discretized. A popular method used in many computational fluid solvers is the *finite volume method*. The finite volume discretization is based on mass conservation of cells in a discretized grid. See the left grid in Figure 1.4 for illustration of a grid. Each grid cell i is associated with saturation values $s_{w,i}, s_{n,i}$ and pressure values $p_{w,i}, p_{n,i}$. The change in the amount of a conserved quantity (here mass) within each grid cell equals the net flux of that quantity across cell faces plus or minus source or sink terms. This finite volume method is implemented in `MRST`, where the conservation equations are discretized using the finite volume approach in space and an implicit first-order discretization in time.

Using superscript n to denote time step and subscripts i and Γ to refer to grid cell and grid faces indices, respectively, the time-implicit finite

volume discretization of equation (2.3) for grid cell i is written as

$$\frac{\phi_i^{n+1}\rho_{\alpha,i}^{n+1}s_{\alpha,i}^{n+1}-\phi_i^n\rho_{\alpha,i}^n s_{\alpha,i}^n}{t^{n+1}-t^n}+\sum_{\Gamma\in\mathscr{F}_i}\rho_{\alpha,\Gamma}^{n+1}v_{\alpha,\Gamma}^{n+1}-\psi_{\alpha,i}^{n+1}=0,\quad \alpha=w,n \tag{2.5}$$

Here t refers to time, $\mathscr{F}_i$ to the set of grid faces bounding cell i, and $v_{\alpha,\Gamma}$ the net volumetric flux of phase α across face Γ where outflow is positive. Under the assumption of isothermal conditions, the density and porosity are functions of pressure, i.e. $\rho_{\alpha,i}^n=\rho_\alpha(p_i^n)$ and $\phi_i^n=\phi_i(p_i^n)$.

The net volumetric fluxes have to be calculated in some way, and in `MRST` they are obtained by discretizing the two-phase extension of Darcy's law (2.2). The simplest way of estimating fluxes across cell faces is to use a scheme known as the *two-point flux approximation* (TPFA) [18]. Let Γ represent the common interface between cells l and k, then the flux from cell l to k across Γ can be approximated as

$$v_{\alpha,\Gamma}^{n+1}=-T_f\lambda_{\alpha,\Gamma}^{n+1}\left[p_{\alpha,k}^{n+1}-p_{\alpha,l}^{n+1}-\rho_{\alpha,\Gamma}^{n+1}g(z_k-z_l)\right] \tag{2.6}$$

Here $\lambda_{\alpha,\Gamma}^{n+1}=\lambda_{\alpha,\Gamma}(s_\Gamma^{n+1},p_\Gamma^{n+1})$ denotes the phase mobility at the interface, z_k and z_l represent the depth value of the respective cell centroids, and T_Γ is the *transmissiblity* associated with face Γ. It is a value related to permeability values and associated cell geometries and is given as the harmonic average of the associated half-face transmissibilities

$$T_\Gamma=\left(\frac{1}{T_{k,\Gamma}}+\frac{1}{T_{l,\Gamma}}\right)^{-1}$$

where the half-face transmissibility $T_{k,\Gamma}$ associated with cell k and face Γ is given as

$$T_{k,\Gamma}=\frac{\boldsymbol{c}_{k,\Gamma}^T\boldsymbol{K}_k\boldsymbol{N}_{k,\Gamma}}{\|\boldsymbol{c}_{k,\Gamma}\|^2}$$

Here, $\boldsymbol{c}_{k,\Gamma}$ represent the vector pointing form centroid of cell k to centroid of face Γ, $\boldsymbol{K}_k$ the permeability tensor of cell k, and $\boldsymbol{N}_{k,\Gamma}$ the area-scaled normal of face Γ, pointing out of cell k. Note that the TPFA scheme is only consitent with Darcy's law (2.2) for so-called K- orthogonal grids, i.e. grids where $\boldsymbol{K}_k\boldsymbol{N}_{k,\Gamma}\|\boldsymbol{c}_{k,\Gamma}$ [18].

All variables in (2.5) are now described, and the number of unknowns can be reduced to two by including the supplementary equations for cell i

$$\begin{aligned}s_{w,i}+s_{n,i}&=1\\ p_{n,i}-p_{w,i}&=p_{cap}(s_{w,i})\end{aligned} \tag{2.7}$$

Therefore equation 2.5 can be solved for either brine saturation and pressure or CO_2 saturation and pressure. Let now $\boldsymbol{s}$ and $\boldsymbol{p}$ refer to the vectors of chosen unknowns associated with either the brine or CO_2 phase, and let $\boldsymbol{x}^{n+1} = [\boldsymbol{s}^{n+1}, \boldsymbol{p}^{n+1}]$ denote the vector of unknowns at time step $n+1$. Since the fluid and rock properties in the scheme generally are non-linear, the implicit scheme given by discretizations (2.5) and (2.6) have to be solved iteratively in order to go from a solution $\boldsymbol{x}^n$ to $\boldsymbol{x}^{n+1}$. It can easily be seen that equation (2.5) and (2.6) combined with possibly boundary conditions and the supplementary equations (2.7) give an equation system that can be expressed on abstract form as

$$\boldsymbol{G}(\boldsymbol{x}^{n+1}, \boldsymbol{x}^n, \boldsymbol{u}^{n+1}) = \boldsymbol{0} \tag{2.8}$$

Here $\boldsymbol{u}^{n+1}$ represents externally imposed controls, which typically related to the source term $\boldsymbol{\psi}_\alpha^{n+1}$. This system can be solved iteratively using e.g. the Newton-Raphson method, which produces a sequence of solutions $\{\boldsymbol{x}_1^{n+1}, ..., \boldsymbol{x}_k^{n+1}, ...\}$ from an initial guess $\boldsymbol{x}_0^{n+1}$ from the scheme

$$\boldsymbol{x}_{k+1}^{n+1} = \boldsymbol{x}_k^{n+1} - \boldsymbol{J}_{\boldsymbol{G}}^{-1}\left(\boldsymbol{x}_k^{n+1}\right)\boldsymbol{G}(\boldsymbol{x}_k^{n+1}, \boldsymbol{x}_k^n, \boldsymbol{u}^{n+1})$$

where $\boldsymbol{J}_{\boldsymbol{G}}(\boldsymbol{x}_k^{n+1})$ denotes the Jacobian of $\boldsymbol{G}$ with respect to $\boldsymbol{x}^{n+1}$. For an good initial guess $\boldsymbol{x}_0^{n+1}$, this sequence will converge to the correct solution. If convergence is not obtained, the time step $t^{n+1} - t^n$ of the simulation has to be shortened.

2.2.2 Vertical Equilibrium (VE) Model

As mentioned in Section 1.1.2, when studying the long-term CO_2 migration process a number of assumptions can be made that greatly reduces the number of unknowns, and thereby drastically reducing the computational requirements to solve the system. The combined assumptions of rapid phase segregation and negligible vertical flow leads to *vertical equilibrium models*, even though the more precise name would be *transverse equilibrium models*. The transverse direction is the direction perpendicular to local aquifer plane. The transversal and vertical direction are not always equal, as an aquifer possibly slopes upwards or downwards. However, in this thesis simulations and analysis are only made on non-sloping aquifers, meaning that the vertical and transverse direction are equal. The terms are therefore used interchangeably and have the same

meaning in this thesis, even thought they in general are different. Likewise are the lateral and horizontal direction also equal in this thesis, and the these terms also used interchangeably.

As mentioned the key assumption of VE models is the presence of equilibrium in the vertical direction. The equilibrium state is characterized by separate brine and CO_2 zones and no vertical flow, i.e. a vertical pressure field in fluid-static equilibrium. If capillary forces are negligible compared to gravity, the brine and CO_2 zones are separated by a *sharp interface*. Otherwise, there will be a *transition zone* of finite thickness, as discussed in 2.1.1.

With vertical equilibrium, the vertical pressure and fluid distribution profiles can always be reconstructed from knowledge of a set of *upscaled* variables that only depend on the lateral position. Upscaled variables refer here to fine-scale variables that have been integrated in the vertical direction. By assuming VE and a known saturation distribution, upscaled variables and parameters can be obtained by integration of the original conservation equation (2.3) in the vertical direction. By doing so, the vertical direction is eliminated from the equation system, reducing the dimensionality of the model from three to two. Although the VE system is two-dimensional, much of the behaviour of the three-dimensional system system is still implicitly captured by the definition of upsscaled variables.

Let now $\zeta_B(x,y)$ and $\zeta_T(x,y)$ denote the aquifer bottom and caprock level, respectively. Given the mass-conservation equation (2.3), assuming immiscible flow and using the multiphase extension of Darcy's law (2.2), the VE formulation is obtained by integrating from aquifer top to bottom along the transversal direction

$$\begin{aligned}\frac{\partial}{\partial t}\int_{\zeta_T}^{\zeta_B} s_\alpha \phi_\alpha \, dz - \int_{\zeta_T}^{\zeta_B} \nabla\cdot\Big(\frac{k_{r,\alpha}}{\mu_\alpha}\boldsymbol{K}(\nabla p_\alpha - \rho_\alpha \boldsymbol{g})\Big)dz \\ = \int_{\zeta_T}^{\zeta_B} \frac{q_\alpha}{\rho_\alpha} dz, \qquad \alpha = w,n\end{aligned} \tag{2.9}$$

The gravity vector $\boldsymbol{g}$ can be decomposed into a lateral $\boldsymbol{g}_\parallel$ and transversal component $\boldsymbol{g}_\perp$, where the lateral component lies in the aquifer plane and the transversal component follows the z-direction with magnitude $g cos\theta$, where θ is the angle between the transversal coordinate axis and the gravity vector $\boldsymbol{g}$. Let $\nabla_\parallel$ denote the lateral component of the del operator, i.e. by letting $\nabla_\parallel = [\partial_x, \partial_y]$, and assume zero flow across the caprock

and bottom boundaries. Leibniz' integral rule can be applied on the second integral to obtain

$$\begin{aligned}\frac{\partial}{\partial t}\int_{\zeta_T}^{\zeta_B} s_\alpha \phi_\alpha dz - \nabla_\parallel \cdot \int_{\zeta_T}^{\zeta_B} \Big(\frac{k_{r,\alpha}}{\mu_\alpha}\boldsymbol{K}(\nabla p_\alpha - \rho_\alpha \boldsymbol{g})\Big)dz \\ = \int_{\zeta_T}^{\zeta_B} \frac{q_\alpha}{\rho_\alpha} dz, \qquad \alpha = w, n\end{aligned} \tag{2.10}$$

By assuming that the tensor $\boldsymbol{K}$ can be decomposed into separate, independent lateral $\boldsymbol{K}_\parallel$ and transversal components $\boldsymbol{K}_\perp$, lateral Darcy flow $\boldsymbol{v}_{\alpha,\parallel}$ will only depend on the lateral pressure gradient. If the upscaled pressure P_α is defined at the caprock level, the fine scale pressure p_α written as

$$p_\alpha(x, y, z) = P_\alpha(x, y) + \rho_\alpha g\big(z - \zeta_T(x, y)\big)cos\theta$$

Inserted into (2.10) this yields

$$\begin{aligned}\frac{\partial}{\partial t}\int_{\zeta_T}^{\zeta_B} s_\alpha \phi_\alpha dz - \nabla_\parallel \cdot \Big[\int_{\zeta_T}^{\zeta_B} \frac{k_{r,\alpha}}{\mu_\alpha}\boldsymbol{K}_\parallel dz\Big]\big(\nabla_\parallel (P_\alpha - \rho_\alpha g \zeta_T) - \rho_\alpha \boldsymbol{g}_\parallel\big) \\ = \int_{\zeta_T}^{\zeta_B} \frac{q_\alpha}{\rho_\alpha} dz, \qquad \alpha = w, n\end{aligned} \tag{2.11}$$

Finally, by introducing a set of upscaled variables, equation (2.11) can be rewritten as

$$\begin{aligned}\frac{\partial}{\partial t}(\Phi S_\alpha) - \nabla_\parallel \cdot \Big[\boldsymbol{\Lambda}_\alpha \kappa\Big(\nabla_\parallel (P_\alpha - \rho_\alpha g cos\theta \zeta_T) - \rho_\alpha \boldsymbol{g}_\parallel\Big)\Big] \\ = \Psi_\alpha, \qquad \alpha = w, n\end{aligned} \tag{2.12}$$

The set of upscaled variables are defined as

$$\begin{aligned}\Phi &= \int_{\zeta_T}^{\zeta_B} \phi dz \\ \boldsymbol{\kappa} &= \int_{\zeta_T}^{\zeta_B} \boldsymbol{K}_\parallel dz \\ S_\alpha &= \Phi^{-1} \int_{\zeta_T}^{\zeta_B} \phi s_\alpha dz \\ \boldsymbol{\Lambda}_\alpha &= \Big(\int_{\zeta_T}^{\zeta_B} \frac{k_{r,\alpha}}{\mu_\alpha}\boldsymbol{K}_\parallel dz\Big)^{-1} \boldsymbol{\kappa}^{-1} \Psi_\alpha \\ &= \int_{\zeta_T}^{\zeta_B} \frac{q_\alpha}{\rho_\alpha} dz\end{aligned}$$

Note here that the upscaled variables are denoted by capital letters, while variables that are defined on the fine scale are denoted by lowercase letters. Variables that have the same interpretation on both scales are denoted by the same letter, like ϕ and Φ, but they may change unit with scale.

Under the assumption of zero residual saturations and a sharp interface between the brine and CO_2 phase, i.e. no capillary fringe, the upscaled saturations S_α and mobilities $\boldsymbol{\Lambda}_\alpha$ are defined for each phase, and can be explicitly expressed in as the following

$$\begin{aligned}
S_n(h) &= \Phi^{-1}\int_{\zeta_T}^{\zeta_T+h}\phi dz \\
S_w(h) &= 1 - S_n(h) \\
\boldsymbol{\Lambda}_n(h) &= \Big(\lambda_{n,e}\int_{\zeta_T}^{\zeta_T+h}\boldsymbol{K}_\parallel dz\Big)\boldsymbol{\kappa}^{-1} \\
\boldsymbol{\Lambda}_w(h) &= \Big(\frac{1}{\mu_w}\int_{\zeta_T}^{\zeta_B}\boldsymbol{K}_\parallel dz\lambda_{w,e}\int_{\zeta_T+h}^{\zeta_T}\boldsymbol{K}_\parallel dz\Big)\boldsymbol{\kappa}^{-1}
\end{aligned}$$

Here h is the height of the CO_2 plume. Similar integrals can be defined for the case with non-negligible residual saturation, but the expressions become more complicated and will involve an additional hysteresis parameter.

As with the fine-scale system the number of unknowns can be reduced with two by including that the upscaled saturations sum to one and using the upscaled capillary pressure function

$$\begin{aligned}
S_n + S_w &= 1 \\
P_n - P_w &= P_{cap}(S_w)
\end{aligned} \tag{2.13}$$

P_n and P_w are used to denote phase pressures at some predefined reference level, often the caprock level. The upscaled capillary pressure is defined as

$$P_{cap}(S_w(h)) = p_{cap,i} + gh(\rho_w - \rho_n)$$

Here $p_{cap,i} = p_{n,i} - p_{w,i}$ is the fine-scale capillary pressure at depth $z = h$. The use of upsacled saturations when expressing and solving VE equations is referred to the *s-formulation*. Another approach is the so-called *h-formulation*, where h is used as an independent unknown instead of

S_n or S_w. The advantage of the *s-formulation* is that the resulting equations are very similar to the original 3D equations, with the only difference being the use of upscaled variables and the dimensional reduction of the simulation domain. The analogy between fine-scale equation (2.3) and (2.12) should be clear, meaning that the VE equation system can be solved using the the same method as presented i subsection 2.2.1. Hence the VE system can also can be solved using 3D simulation code with some modest modifications.

2.2.3 Hybrid Model

Description

A hybrid model is a combination of a fine-scale 3D and upscaled VE model. Therefore there is an assumption of vertical equilibrium in some part of the domain. Figure 2.6 illustrates how the computational grid can be split up into two parts, which from now on is referred to as the 3D (yellow cells) and VE (blue cells) domain. Hybrid models are currently being developed at the Department of Scientific Computing at SINTEF Digital and it is expected that they will publicly available in one of the next versions of `MRST-co2lab` [1].

In the 3D domain the flow is determined by the equation system given by (2.3) and (2.4), while in the VE domain the flow is determined by (2.12) and (2.13). The discretization of the 3D model (2.5) can alternivaly be written as

$$\frac{1}{t^{n+1}-t^n}\left[\left(\boldsymbol{\phi}\boldsymbol{\rho}_\alpha \boldsymbol{s}_\alpha\right)_i^{n+1} - \left(\boldsymbol{\phi}\boldsymbol{\rho}_\alpha \boldsymbol{s}_\alpha\right)_i^{n}\right] + \sum_{j\in V(i)} f_{ij}(\boldsymbol{p}_\alpha^{n+1}, \boldsymbol{s}_\alpha^{n+1}) = \psi_{\alpha,i}^{n+1} \qquad \alpha = w,n \tag{2.14}$$

where $V(i)$ is the set of neighbouring cells to cell i and f_{ij} is the mass flux from cell i to j, i.e. f_{ij} is greater then zero when the net mass flux is from cell i to j. Similarly, the discretization of (2.12) can be given as

$$\frac{1}{t^{n+1}-t^n}\left[\left(\boldsymbol{\Phi}\boldsymbol{\rho}_\alpha \boldsymbol{S}_\alpha\right)_i^{n+1} - \left(\boldsymbol{\Phi}\boldsymbol{\rho}_\alpha \boldsymbol{S}_\alpha\right)_i^{n}\right] + \sum_{j\in V(i)} f_{ij}(\boldsymbol{P}_\alpha^{n+1}, \boldsymbol{S}_\alpha^{n+1}) = \Psi_{\alpha,i}^{n+1} \qquad \alpha = w,n \tag{2.15}$$

[1] New and old releases of `MRST` can be found at `http://www.sintef.no/projectweb/mrst/downloadable-resources/download/`

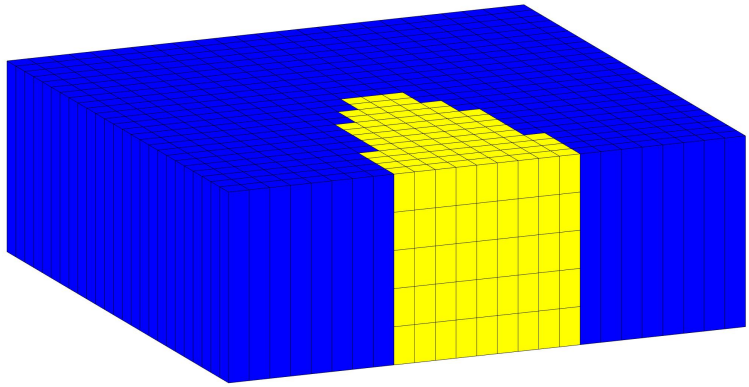

Figure 2.6: Illustration of a hybrid grid. The yellow and blue cells represent the 3D and VE domain, respectively. Note the lack of explicit vertical discretization in the VE domain.

System (2.14) and (2.15) are on the same form, only with different interpretation of the variables, giving that they can be solved simultaneously using already existing solvers in `MRST`. However, special attention has to be made to the interfaces between the domains of different discretization. Or more explicitly, the flux f_{ij} between cells i and j belonging to different discretizations regions have to be modelled explicitly. In this thesis this is limited to flux between VE and 3D regions.

Flux between a VE and 3D domain is solved by introducing virtual cells. Figure 2.7 shows how an interface between a 3D and VE region is modelled using virtual cells within the VE region. In this section superscript tilde is used to represent parameters defined in the virtual cells. If saturation and pressure within these virtual cells can be determined, the fine-scale volumetric flux can be determined using the 3D formulation given equation (2.6).

Under the assumption of VE and a sharp interface, the CO_2-brine interface in VE cell i will lie at depth $z_{si} = HS_{n,i}$. This interface is most likely to be within a virtual cell i_k, see Figure 2.7.As this thesis only consider the injection process, the cell above and below i_k has brine saturation equal $s_{r,w}$ and 1, respectively. As the saturation value is defined at the centroid of the cell, the brine saturation is here defined as

$$\widetilde{s}_{w,i_k} = s_{r,w} + \frac{1 - s_{r,w}}{z_B - z_T}(z - z_T)$$

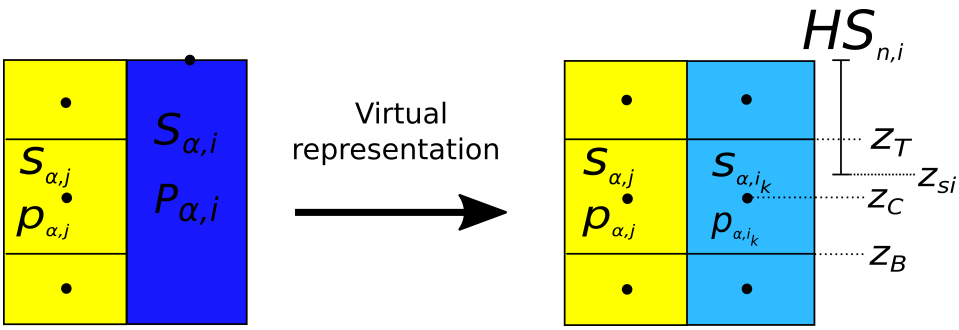

Figure 2.7: Illustration of how a VE disretized cell is virtually represented. Yellow cells belong to the 3D discretization, dark blue to the VE discretization and the light blue are 3D virtual cells. A VE cell i is discretized into a number n_i of virtual cells $i_1,...,i_k,...i_{n_i}$. The black bullets show where the variables are defined.

Here z_T and z_B denote the value of the z-coordinate at the top and bottom interface of virtual cell i_k, as illustrated in Figure 2.7. The virtual CO_2 saturation is given as $\widetilde{s}_n = 1 - \widetilde{s}_w$.

The value of the upscaled pressures P_α are defined at the top of the VE column. If z_{cr} defines the caprock level, the fine-scale pressure at the centroid of a cell z_C is under the assumption of constant phase densities given as

$$\widetilde{p}_{w,i_k} = P_{w,i} + \int_{z_{cr}}^{z_C} \left(\rho_w \widetilde{s}_w + \rho_n \widetilde{s}_n\right) g \, dz$$

Coupled System

The equations of a hybrid model can be written in compact form. Let V_{3D} and V_{VE} denote the set of cells that are in the 3D and VE discretization, respectively. Using the similarity of (2.14) and (2.15), the discretization of the coupled system can now be written as

$$\frac{1}{t^{n+1} - t^n}\left[\left(\boldsymbol{\rho}_\alpha \boldsymbol{\Theta}_\alpha\right)_i^{n+1} - \left(\boldsymbol{\rho}_\alpha \boldsymbol{\Theta}_\alpha\right)_i^{n}\right] + \sum_{j \in V(i)} f_{ij}(\boldsymbol{\Upsilon}_\alpha^{n+1}, \boldsymbol{\Pi}_\alpha^{n+1}) = \Xi_{\alpha,i}^{n+1}, \quad \alpha = w, n$$

where the hybrid variables is dependent on the discretization as

$$\Pi_{\alpha,i} = \begin{cases} p_{\alpha,i}, \text{ if } i \in V_{3D} \\ P_{\alpha,i}, \text{ if } i \in V_{VE} \end{cases} \qquad \Upsilon_{\alpha,i} = \begin{cases} s_{\alpha,i}, \text{ if } i \in V_{3D} \\ S_{\alpha,i}, \text{ if } i \in V_{VE} \end{cases}$$

$$\Theta_i = \begin{cases} \phi_i, \text{ if } i \in V_{3D} \\ \Phi_i, \text{ if } i \in V_{VE} \end{cases} \qquad \Xi_{\alpha,i} = \begin{cases} \psi_{\alpha,i}, \text{ if } i \in V_{3D} \\ \Psi_{\alpha,i}, \text{ if } i \in V_{VE} \end{cases}$$

The mass fluxes f_{ij} are diviveded into three cases; (i) coupling between two fine-scale cells, (ii) coupling between two coarse-scale cells and (iii) coupling between the two types of discretizations

$$f_{ij}(\Upsilon_i, \Pi_i, \Upsilon_j, \Pi_j) = \begin{cases} f_{ij}(s_i, p_i, s_j, p_j), & \text{if } i,j \in V_{3D} \\ f_{ij}(S_i, P_i, S_j, S_j), & \text{if } i,j \in V_{VE} \\ f_{ij}(s_i, p_i, S_j, P_j), & \text{if } i \in V_{3D}, j \in V_{VE} \end{cases}$$

The supplementary equations are given as

$$\Upsilon_{w,i} + \Upsilon_{n,i} = 1$$

$$\Pi_{n,i} - \Pi_{w,i} = \begin{cases} p_{cap}(s_{w,i}), & \text{if } i \in V_{3D} \\ P_{cap}(S_{w,i}), & \text{if } i \in V_{VE} \end{cases}$$

Separation Radius

An important question in a hybrid model is how the VE and 3D domain is determined. This choice can be influenced by a great number of factors, like fluid and rock properties, slope of the aquifer, impermeable layers, injection rate etc. The natural choice is to have a fine-scale 3D model in areas with significant vertical flow and a VE model in all other areas. *Near-well areas* are here identified as areas close to injecting wells where the VE assumption does not hold. Therefore, a hybrid model could have a 3D domain within a radius of the vertical wells and VE domain in all other areas. As this radius separates the VE and 3D domain it is named the *separation radius* R^*. The VE and 3D domain in a hybrid model might change under a simulation, and therefore the separation radius is in general time-dependent, $R^* = R^*(t)$. Figure 2.8 illustrates some possible choices of separation functions.

In a numerical simulation the solution is computed at different time steps. Therefore the separation functions will actually be stair step functions where intervals are given by the time steps in the simulation. At

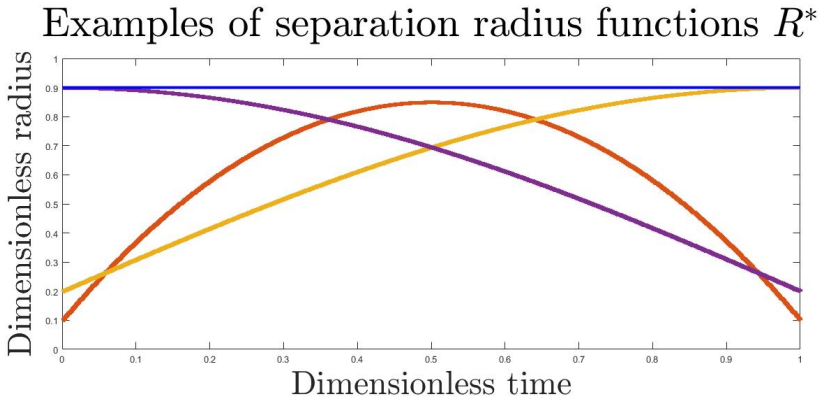

Figure 2.8: Examples of separation radius functions $R^*(t)$.

each time step the hybrid model has to be redefined if the separation radius changes. Depending on the simulation scenario, it may be overly complex to constantly change the hybrid model set up. An alternative approach would be to set the boundary so far away from the well that it encompasses the maximum separation radius will be achieved. This corresponds to the constant blue line in Figure 2.8.

2.3 Determination of near-well Area

In a hybrid model there is an interface between the 3D domain and the VE domain. In this thesis it is assumed that the interface lies at a radius R^* from an injecting well. Hence, the determination of the near well area focuses on finding a function $R^* = R^*(t)$ that determines how far out from a well one has to move before the vertical equilibrium assumptions holds.

In [20] the authors examined the applicability of VE and sharp interface assumptions in modelling of CO_2 sequestration. As CO_2 invades the aquifer and creates the CO_2 plume, the brine needs to drain vertically before the two phases are completely segregated. The article concluded that this *drainage time*, relative to the time scale of the simulation, determines the applicability of the vertical equilibrium assumption.

In addition to brine drainage, this thesis also assumes that the horizontal flux of CO_2 has an influence of the vertical equilibrium assumption. If the vertical flux of CO_2 is small compared to the horizontal flux of CO_2, the system is dominated by the horizontal flow and this strengthens

the vertical equilibrium assumption.

Inspired by this, this thesis considers the ratio of vertical volume flux of brine to horizontal volume flux of CO_2 to determine if the VE assumption holds. More precisely, the *flux ratio number* η is calculated to determine if a column at some radius r can be assumed to be in vertical equilibrium. The flux ratio number is defined as

$$\eta(r,t) = \frac{f_\perp(r,t)}{f_\parallel(r,t)} \tag{2.16}$$

Here $f_\perp$ is the mean vertical volume flux of brine and $f_\parallel$ is the mean horizontal volume flux of CO_2 within the CO_2 plume.

$$f_\perp(r,t) = \frac{1}{h(r,t)} \int_{\zeta_T}^{\zeta_T+h(r,t)} f_{\perp,w}(z,r,t)\,dz \tag{2.17}$$

$$f_\parallel(r,t) = \frac{1}{h(r,t)} \int_{\zeta_T}^{\zeta_T+h(r,t)} f_{\parallel,n}(z,r,t)\,dz \tag{2.18}$$

Here $h(r,t)$ is the height of the CO_2 plume, $f_{\perp,w}$ is the volume flux of brine in the vertical direction and $f_{\parallel,n}$ is the volume flux of CO_2 in the horizontal direction.

If the ratio η is above some threshold value $\overline{\eta}$ this should be interpreted as significant vertical flow of brine compared to horizontal flow of CO_2, such that a column cannot be assumed to be in vertical equilibrium. The smaller the threshold value is, the more restrictive is the VE assumption. The separation radius at time t is then taken to be the largest radius at which $\eta(r,t) > \overline{\eta}$.

This thesis presents one numerical and one analytical approach for determining R^*. The numerical approach uses vertical and horizontal volume fluxes along internal cell faces computed from a 3D simulation, while the analytic approach is based on an analytic result of the interface position between CO_2 and brine presented in [21].

2.3.1 Numerical Approach

The 3D discretized equations is solved using a finite volume method. Between all time steps in the simulation, the volume rate (unit m^3s^{-1}) in and out of the internal cell faces is computed. For a column at a radius r

from an injecting well with a set of cells $V(r)$ in the CO_2 plume, the mean vertical and horizontal volume flux can then be computed as

$$f_{\perp}(r,t) = \frac{1}{h(r,t)} \sum_{i \in V(r)} h_i \frac{f^V_{\perp,i}(r,t)}{A_{\perp,i}}$$
$$f_{\parallel}(r,t) = \frac{1}{A(r,t)} \sum_{i \in V(r)} f^V_{\parallel,i}(r,t)$$

Here $f^V_{\perp,i}$ is the volume rate of CO_2 out of the face of cell i with normal in the vertical direction (bottom faces in Figure 2.9), $A_{\perp,i}$ is the areal of the face with normal in vertical direction, $f^V_{\parallel,i}$ is the volume rate of brine out of the face of cell i with normal in the radial direction (right faces in Figure 2.9) and $A_{\parallel}(r,t)$ is the total areal of the faces with normal in the radial direction within the CO_2 plume, i.e. $A_{\parallel}(r,t) = \sum_{i \in V(r)} A_{\parallel,i}$.

From this the flux ratios $\eta(r,t)$ are computed numerically and the separation radius is then taken to be

$$R^*(t) = \underset{r}{\operatorname{argmax}} \{ r \mid \eta(r,t) > \overline{\eta} \}$$

2.3.2 Analytical Approach

Test Case Description

This analytical approach is built on the analytical solution giving the height of the CO_2 plume for a specific fluid-rock system presented in [21]. The solution is given for a simple, vertical injection scenario, which will be referred to as the *test case* throughout this thesis.

The test case consist of a single, vertical well situated at the center of a cubic aquifer with height H. The aquifer is originally filled with brine, and the well is injecting equal amounts of CO_2 along the whole depth of the aquifer. The porosity and permeability of the aquifer is homogeneous, and the aquifer has zero slope. The aquifer is sealed at the top and bottom (no-flow boundary conditions), and open to flow through lateral boundaries (fixed pressure boundary conditions). The fluid viscosities and densities are assumed to be constant, i.e. the compressibilities are zero. The rock compressibility c_ϕ is also zero and for simplicity the residual saturations $s_{r,\alpha}$ are also assumed to be zero. It also assumed the there is a sharp interface between the brine and CO_2 phase, i.e. the capillary pressure p_{cap} is zero.

As the well is at the center of the aquifer and the porosity and permeability is homogeneous, the flow is radially symmetric around the well. Therefore the simulations can be conducted in the (r, z, t)-space instead of the (x, y, z, t)-space, and the cubic grid can be reduced to a thin slice, as shown in Figure 2.9. If the volumetric injection rate of the well is Q, the injection rate of CO_2 into the slice with angle ω is equal $Q_\omega = \frac{\omega}{2\pi}Q$. The red cells in this figure shows where the well is centred.

Analytical Mean Horizontal Flux

When viscous forces dominate gravity forces the plume height $h(r, t)$ in the test case is given as [21]

$$h(r,t) = \begin{cases} H, & \text{for } \chi \le 2/\lambda \\ \frac{H}{\lambda - 1}\left(\sqrt{\frac{2\lambda}{\chi}} - 1\right), & \text{for } 2/\lambda < \chi \le 2\lambda \\ 0, & \text{for } \chi > 2\lambda \end{cases} \tag{2.19}$$

Here χ and λ are dimensionless parameters defined as

$$\chi = \frac{2\pi H \phi (1 - s_{r,w})}{Q} \frac{r^2}{t} \qquad \lambda = \frac{\lambda_n}{\lambda_w}$$

λ is known as the mobility ratio, where the relative permeability values of brine and CO_2 is evaluated at different saturation values. The mobility of brine is defined ahead of the interface, while CO_2 is defined behind, such that $\lambda = \frac{k_{r,n}(1-s_{r,w})/\mu_n}{k_{r,w}(1)/\mu_w}$. Figure 2.10 illustrates how the solution looks like at some time t.

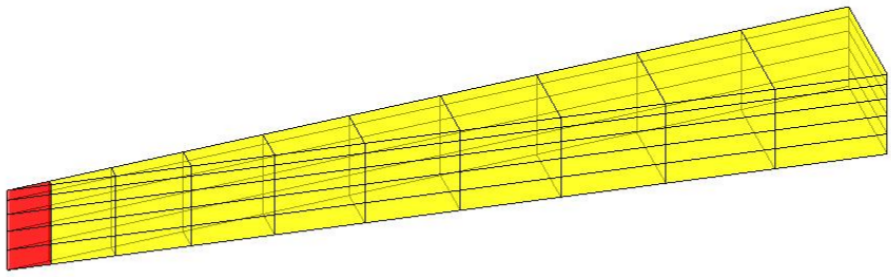

Figure 2.9: Reduced 3D aquifer grid of test case. The red cells indicates that the well is situated at the center of the aquifer and that the well is injecting CO_2 in the whole depth of the aquifer.

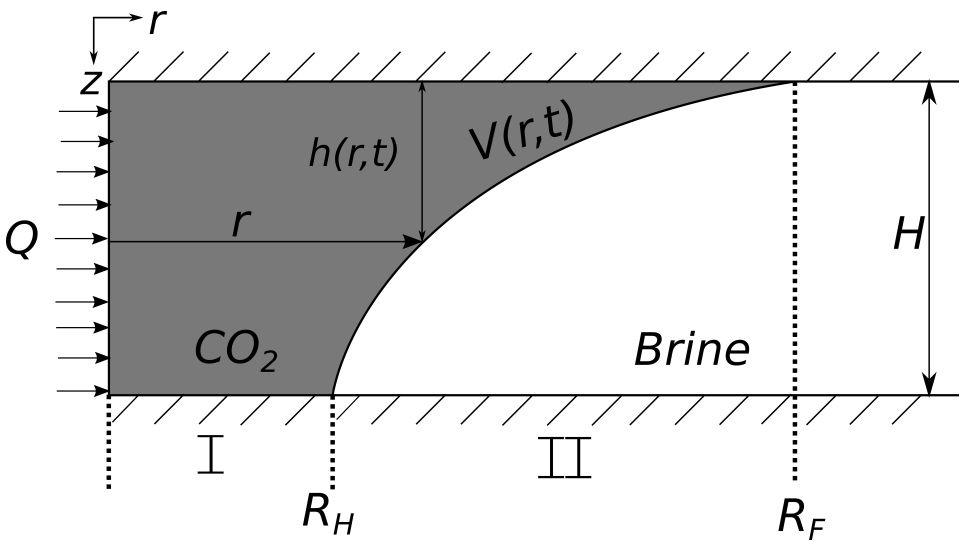

Figure 2.10: Illustration of how the analytical plume height (2.19) looks like at some time t. The CO_2 fully fills the aquifer height H i region I up to the radius R_H. R_F is the front radius of the plume, and region II is defined as $r \in (R_H, R_F]$

From this analytical solution the mean horizontal volume flux of CO_2 $f_\parallel(r,t)$ can be computed. The analytical flux is different region I and II in Figure 2.10. The regions are defined by the radii R_H and R_F, and they are found by setting $\chi = 2/\lambda$ and $\chi = 2\lambda$, respectively. If $\beta = \frac{\pi H \phi (1-s_{r,w})}{Q}$, the radii are given as

$$R_H(t) = \sqrt{\frac{t}{\beta\lambda}} \qquad R_F(t) = \sqrt{\frac{\lambda t}{\beta}}$$

Assume first that r is in region II. The volume of CO_2 outside of radius r is denoted $V_{II}(r,t)$ and is given as

$$\begin{aligned} V_{II}(r,t) &= 2\pi\phi(1-s_{r,w}) \int_r^{R_F} h(r',t) r' dr' \\ &= 2\pi\phi(1-s_{r,w}) \frac{H}{\lambda - 1} \int_r^{R_F} \left(\sqrt{\frac{2\lambda}{\chi}} - 1 \right) r' dr' \\ &= \frac{2\pi H \phi (1-s_{r,w})}{\lambda - 1} \int_r^{R_F} (R_F - r') dr' \\ &= \frac{H\pi\phi(1-s_{r,w})}{\lambda - 1} (R_F - r)^2 \end{aligned}$$

The total volume flux $F(r,t)$ out of the cylinder with radius r and height $h(r,t)$ is then equal

$$F_{II}(r,t) = \frac{d}{dt}V_{II}(r,t) = \frac{H\pi\phi(1-s_{r,w})}{\lambda-1}\frac{(R_F-r)R_F}{t}$$

This band at r has areal $A_{II}(r,t) = 2\pi r h(r,t) = \frac{2\pi H}{\lambda-1}(R_F(t)-r)$, and the mean volume flux is then given as $F_{II}(r,t)/A_{II}(r,t)$.

If r is in section I, the mean volume flux is trivial to find. As the volumetric injection rate is Q and the well is injecting equal amounts along the whole depth H of the aquifer, the volume rate of CO_2 that crosses the cylinder band at r in section I is simply equal Q. Finally, by using that $s_{r,w} = 0$ for simplicity in this thesis, the analytical mean horizontal flux is given as

$$f_{\parallel}(r,t) = \begin{cases} \frac{Q}{2\pi H r}, & \text{for } r \in [0, R_H] \\ \frac{\phi R_F(t)}{2t}, & \text{for } r \in (R_H, R_F] \end{cases} \tag{2.20}$$

Note that the flux in region II is independent of the radius r.

Relation Horizontal and Vertical Flux

If the analytical mean vertical flux $f_{\perp}(r,t)$ was known too, this could have been used to calculate the flux ratio number η directly as in the numerical approach using (2.16). However, this is not known and a different approach has to be made. Since the question is whether a given column can be assumed to be in vertical equilibrium, this is in fact an one-dimensional problem. For incompressible one dimensional two-phase flow in a porous medium, the volume flux of CO_2 is given as [22]

$$v_w = \frac{\lambda_w}{\lambda_n+\lambda_w}v + \frac{\lambda_n\lambda_w}{\lambda_n+\lambda_w}k\gamma + k\frac{\lambda_n+\lambda_w}{\lambda_n\lambda_w}\frac{\partial p_{cap}}{\partial z} \tag{2.21}$$

Here is $v = v_n + v_w$ the total volume flux (where v_α is given from the one dimensional form of Darcy's law (2.2)), $\gamma = (\rho_n - \rho_w)g$ the difference in specific weight and k the absolute permeability. As a column is assumed to be in VE if $\eta \le \overline{\eta}$, the vertical flow has to fulfil the following equation for the VE assumption to hold

$$f_{\perp} \le \overline{\eta} f_{\parallel}$$

This gives the *maximum value* the mean vertical flux $f_\perp^{max}$ can take for a column to be considered to be in vertical equilibrium. If the VE assumption holds, the mean flux $f_\perp$ is possibly less than $f_\perp^{max}$. However, this analytical approach aims for rather *overestimating* than underestimating the separation radius, and therefore assumes that when the VE assumption holds the mean vertical flux is exactly equal

$$f_\perp^{max} = \overline{\eta} f_\parallel$$

Under the assumption of a sharp interface, which is consistent with negligible capillary pressure, the last term in (2.21) is neglected. Around a well in the fluid-rock system described most flux will be horizontal driven by a high pressure in the well. Therefore, as v is small in the vertical direction, the first term can also be neglected. As the vertical volume flux (2.21) now is a function of saturations, the brine saturation level that corresponds to the maximum mean vertical flux $f_\perp^{max}$ can be determined from the following equation

$$k\gamma \frac{\lambda_n(1-s_w)\lambda_w(s_w)}{\lambda_n(1-s_w)+\lambda_w(s_w)} = \overline{\eta} f_\parallel(r,t) \tag{2.22}$$

As the k_r-s relationships often are non-linear, this equation has to be solve numerically. Let the solution be denoted as the *characteristic saturation level* s_w^*. The reason to denote the solution as the characteristic level, is that characteristics will be used to determine if the column at radius r can be assumed to be in VE.

Characteristic Analysis

An aquifer is initially fully filled with brine. As the vertical equilibrium assumption builds upon that brine and CO_2 are separated, it is here examined how long time it takes for brine to flow downwards from the caprock through a CO_2 plume with height $h(r,t)$. Let this time be denoted as the *segregation time* $t^* = t^*(r,t)$. If the segregation time t^* is greater then the time since the injection start t, one cannot assume vertical equilibrium. In order to find $t^*(r,t)$ for a given height $h(r,t)$, it has to be known how fast brine flows downwards.

For incompressible fluids and incompressible rock, mass conserva-

tion of brine in the vertical direction can be written as [22]

$$\phi\frac{\partial s_w}{\partial t} + v\frac{\partial}{\partial z}\Big(k\frac{\lambda_w}{\lambda_w+\lambda_n}\Big) + \gamma\frac{\partial}{\partial z}\Big(k\frac{\lambda_n\lambda_w}{\lambda_w+\lambda_n}\Big) + \frac{\partial}{\partial z}\Big(k\frac{\lambda_n\lambda_w}{\lambda_w+\lambda_n}\frac{\partial p_{cap}}{\partial z}\Big) = 0 \tag{2.23}$$

This equation actually follows directly from (2.21), which gives the flux term in the mass conservation equation. Therefore, under the assumption of a sharp interface and large horizontal flux compared to vertical flux, the second and last term in (2.23) is neglected. The one dimensional mass conservation equation with $u = s_w$ can now be written as

$$\frac{\partial u}{\partial t} + \frac{\partial g(u)}{\partial z} = 0 \tag{2.24}$$

This is known as the scalar hyperbolic conservation law [23], and $g(u) = \frac{k\gamma}{\phi}\frac{\lambda_n\lambda_w}{\lambda_w+\lambda_n}$ is known as the *flux function* and $u = u(z,t)$ as the density of the conserved quantity. Assuming that the flux function can be differentiated, equation (2.24) can be rewritten as

$$\frac{\partial u}{\partial t} + g'(u)\frac{\partial u}{\partial z} = 0$$

$g'(u)$ is known as the *characteristic speed* and Figure 2.11 presents an example plot of the characteristic speed for a cubic k_r-s relationship, absolute permeability 10mD and fluid and rock properties given i Tabular 3.1, which are the parameters that analytical results are conducted from in Section 3.2.2. If the initial solution $u_0 = u(z,0)$ is known at a point z_0 the solution will propagate along the line

$$z = z_0 + g'(u_0(z_0))\,t$$

Thus, if the initial saturation profile s_w is known along a vertical column, the characteristic speeds can be used to find out how the initial solution propagates. The saturation profile is not known, but the limit value of s_w^* for the VE assumption to hold is known from equation (2.22).

The analytical vertical volume flux is plotted in Figure 2.12 for fluid and rock properties given in Tabular 3.1, absolute permeability 10 mD and cubic k_r-s relationships. From this figure it is clear that equation (2.22) in fact might have two solutions, one to the left and one to right of the maximal point. The characteristic saturation level s_w^* should be

taken as the smallest value that solves (2.22), as this gives a positive characteristic speed that goes downwards in the plume, which can be seen from Figure 2.11. The other of solution of (2.22) corresponds to a negative characteristic speed going upwards, which is not where the interest in this thesis lies. In addition if $\max(f_\perp) < \overline{\eta} f_\parallel(r,t)$, a solution to (2.22) cannot be found, which is interpreted as a large horizontal flux such that the column at radius r can be assumed to be in VE.

For a column at radius r it is assumed that the characteristic brine saturation s_w^* starts to propagate downwards from the caprock level at the time where the plume first reaches the radius. In a reality CO_2 and and brine starts to segregate immediately after CO_2 is injected into the aquifer. However, it is not known how far the segregation process has come when the plume first reaches r. E.g. there might be some brine left in the whole plume height or there might some brine left just in the bottom of the plume. As this analytical approach aims to overestimate the segregation time, it is assumed that the segregation at the radius r first starts at the time when the plume reaches r. Let us denote this time as the *front time* $t_F = t_F(r)$. This time is found by setting $\chi = 2\lambda$, which gives

$$t_F = \frac{\beta}{\lambda} r^2$$

Finally, the segregation time for brine through the CO_2 plume at radius r and time t with height $h(r,t)$ is given as

$$t^*(r,t) = t_F(r) + \frac{h(r,t)}{v^*} \tag{2.25}$$

$v^* = g'(s_w^*)$ is the characteristic speed given at the characteristic saturation level. In fact the speed v^* could be equal the characteristic speed $g'(s_w^*)$ or a shock speed given by the Rankine-Hugoniot condition [23].

It is assumed that at the caprock level the brine saturation is equal s_w^*. The brine saturation profile downwards in the plume is unknown, but it is here assumed that the saturation is always less then 0.5. Oppositely, if $s_w > 0.5$ this corresponds to that there is more brine than CO_2 in the CO_2 plume and that the slow drainage process of brine has not started. In Figure 2.12 the analytical vertical flux function was plotted for relevant scenario parameters. For this set of parameters the flux function can be separated into to two convex parts, for $s \in [0, 0.52) \cup (0.79, 1]$, and one concave part, for $s \in (0.52, 0.79)$. As it is assumed that $s_w < 0.5$ in the

whole depth of the CO_2 plume, the vertical flux is always in the convex domain of the analytical vertical flux function. Therefore the brine saturation profile propagates for what is known as a *rarefaction wave* [23] and not as a shock wave. In summary, for other scenarios with different flux function the speed v^* could be equal a shock speed, but in thesis the speed is always equal $g'(s_w^*)$.

If $t^* > t$, the brine and CO_2 at radius r have not had time to fully separate, meaning that the column at r cannot be assumed to be in VE. As all plume heights at a distance r is associated with a segregation time $t^*(r,t)$, this method is used to find a radius $R^*(t)$ that separates the domain into one part where the VE assumption holds and one part where the fine-scale 3D simulation should be carried out. The value of $R^*(t)$ is given as the maximum radius r at which $t^*(r,t)$ from (2.25) is greater then the time step t .

$$R^*(t) = \underset{r}{\operatorname{argmax}} \{ r \mid t^*(r,t) > t \}$$

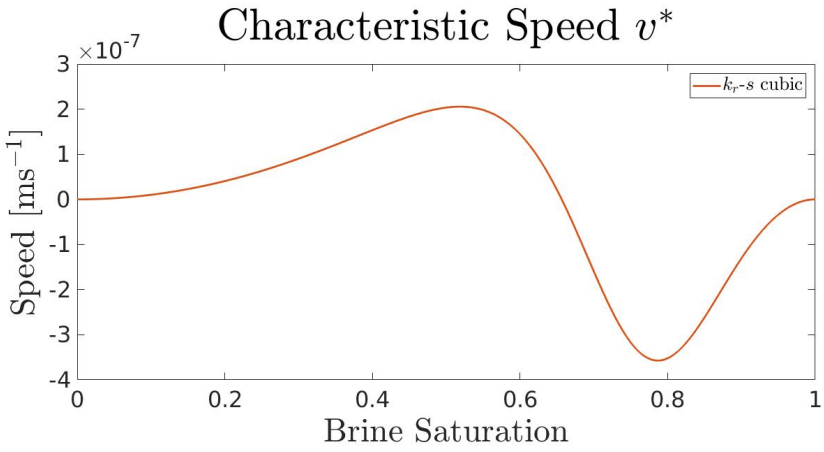

Figure 2.11: Characteristic speeds for cubic relative permeability curves.

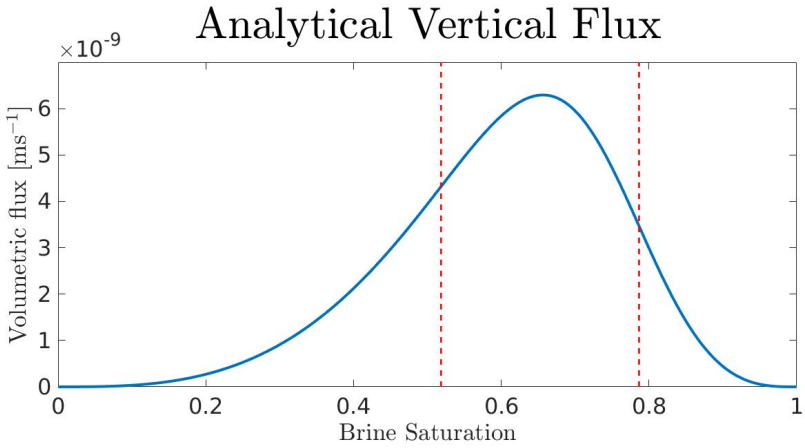

Figure 2.12: Example of analytical vertical flux for cubic relative permeability curves. The red dashed lines give the turning points of the function, i.e. the function is concave between the red lines and convex for the leftmost of rightmost part.

Chapter 3

Numerical Results and Discussion

In this chapter numerical results are presented and discussed. This chapter consists of three sections. The first section illustrates the benefits, drawbacks and differences of 3D and VE simulations with basis in three test cases. The second section covers determination of the near-well area by the analytical and numerical approach. The last section presents results from hybrid simulations and compares these results with full 3D and VE simulations. Each section is closed by a discussion part.

3.1 VE and 3D Simulations

In Section 1.1.2, it was described that the vertical equilibrium assumption does not hold in the vicinity of a well. In [20] the authors considered the applicability of the vertical equilibrium assumption in CO_2 sequestration modelling, and concluded that the applicability of a vertically-integrated modelling approach depends on the time scale of the vertical brine drainage within the plume, relative to the time scale of the simulation. Inspired by this, numerical simulations where conducted on the test case to visualize how rock and fluid properties influence VE and 3D simulations.

Simulations were conducted on three test cases, denoted test case A, B and C, fulfilling the properties of the original test case described in Section 2.3.2. A specification of equal simulation parameters are given in Tabular 3.1, while different parameters for the test cases are given in Tabular 3.2.

Equal Properties	
Porosity	0.10
Rock compressibility	0
Aquifer height	15 m
Aquifer Radius	5000 m
Brine density	1000 kg m^{-3}
CO_2 density	720 kg m^{-3}
Brine compressibility	0
CO_2 compressibility	0
Brine viscosity	8.0×10^{-4} Pa s
CO_2 viscosity	6.0×10^{-5} Pa s
Residual saturation brine	
Residual saturation CO_2	0
Annual injection rate	0.1 Mt
$p_{cap}(s_w)$	0

Table 3.1: Equal scenario parameters for test cases that examines differences between VE and 3D simulation.

Test Case	Absolute permeability	$k_{r,w}$	$k_{r,n}$
A	100 mD	Linear	Linear
B	50 mD	Quadratic	Quadratic
C	10 mD	Cubic	Cubic

Table 3.2: Different scenario parameters for test case A, B and C.

3.1.1 Numerical Results

Figure 3.1, 3.2 and 3.3 show CO_2 saturation after 15 years of injection in test case A, B and C, respectively. The VE simulation computes upscaled variables for each grid column, but the plotted values are the upscaled saturation S_n reconstructed into fine-scale saturation values for each cell in the 3D discretization using the plume height h as shown in the Section 2.2.3. As seen in these figures, there is almost no differences in VE and 3D results for test case A and B, while for test case C there are significant differences. In test case C, the vertical flow of CO_2 is much greater in the VE simulation than in the 3D simulation. Also, the lateral flow of CO_2 in the 3D simulation is greater than in the VE simulation, and this results in the great difference in the shape of the CO_2 plumes.

Figure 3.1, 3.2 and 3.3 only show CO_2 saturation at one simulation time step. By defining the *mean saturation difference* δ_{sat} as

$$\delta_{sat} = \frac{1}{V_{tot}} \sum_{i \in V_{3D}} \delta_{sat,i} V_i$$

the saturation difference of the VE and 3D simulation is quantified. Here V_{tot} is the total pore volume of the aquifer, V_{3D} is the set of cells in the 3D discretized grid, $\delta_{sat,i}$ is the absolute value of the difference in CO_2 saturation in 3D cell i between the 3D and reconstructed VE value and V_i is the pore volume of 3D cell i. Figure 3.4 shows the mean saturation difference for the three test cases throughout 25 years of injection. From this plot it is even more clear that the VE and 3D simulations in test case A and B are almost identical, while the simulations in test case C are quite different.

Tabular 3.3 presents the total simulation time for the VE and 3D model in the test cases, and the simulation time of the VE model is for all cases under 6,5 % of time of the corresponding 3D simulation. Note that simulation times are only included to show difference between model types, and not included for discussion on fastness and efficiency of the numerical solver. It is also worth to mention that the numerical solver used in `MRST` is not optimized for computational speed.

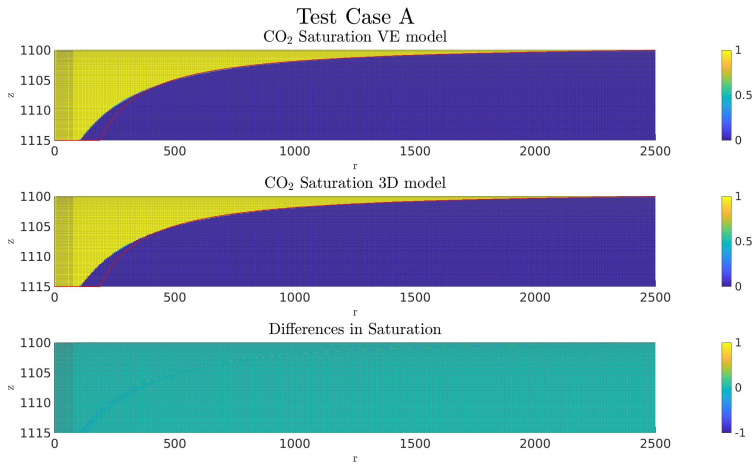

Figure 3.1: The two top plots show CO_2 saturation computed using a VE and 3D model after 15 years of injection giving scenario parameters as in test case A. The red line plots the analytical plume height given in equation (2.19). The bottom plot shows the saturation difference for each grid cell from the two simulations.

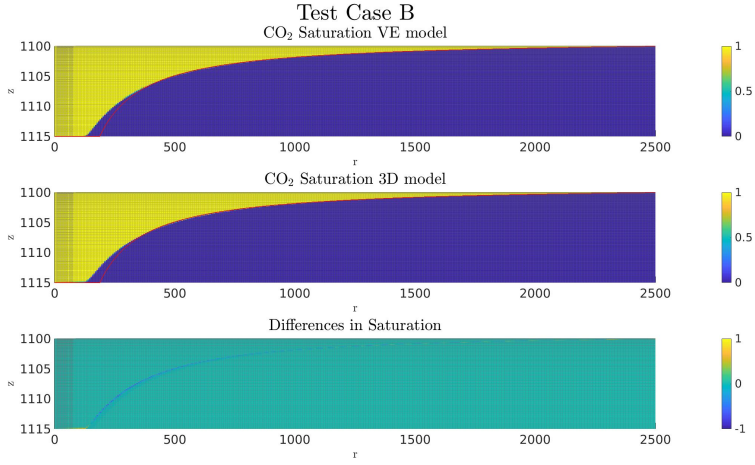

Figure 3.2: The two top plots show CO_2 saturation computed using a VE and 3D model after 15 years of injection giving scenario parameters as in test case B. The red line plots the analytical plume height given in equation (2.19). The bottom plot shows the saturation difference for each grid cell from the two simulations.

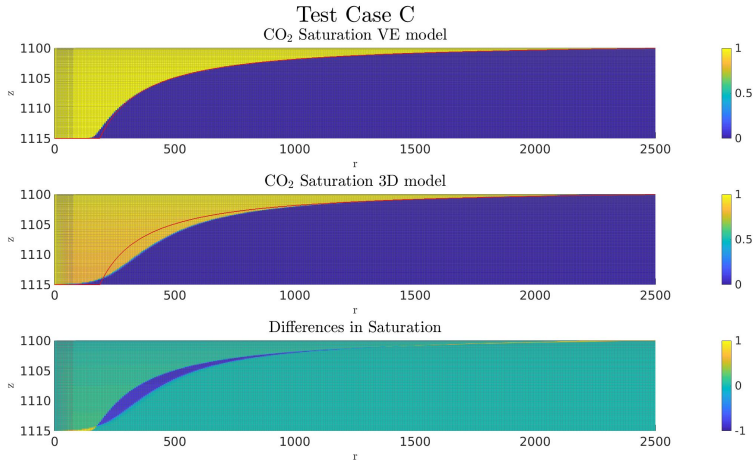

Figure 3.3: The two top plots show CO_2 saturation computed using a VE and 3D model after 15 years of injection giving scenario parameters as in test case C. The red line plots the analytical plume height given in equation (2.19). The bottom plot shows the saturation difference for each grid cell from the two simulations.

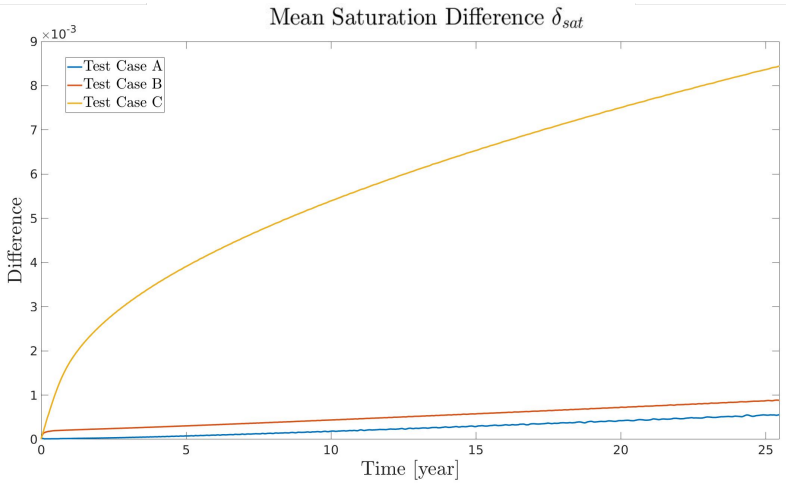

Figure 3.4: The mean cell difference in CO_2 saturation for the three test cases for 25 years of injection.

3.1.2 Discussion

The equality of the simulations in test case A and B is due to the fact that the vertical brine drainage is much faster here than in test case C. This is also is in accordance with the conclusion from [20], where the authors stated that the k_r-s relationship has a large impact on the time scale of the brine drainage and hence whether CO_2 and brine segregate fully on the time scale of interest. This is better understood by examining the plot of theoretical relative permeability curves in Figure 2.4. As brine saturation decreases asymptotically to zero, the cubic relative permeability curve decreases more rapidly than the linear and quadratic curves, leading to a significant slower drainage of brine from the CO_2 plume. Thus brine will flow slower within the CO_2 plume in test case C than in test case A and B, resulting in that brine and CO_2 will not separate quickly enough for the VE assumption to hold. To sum up, these results clearly show that in some scenarios the significantly faster VE model can be used, while for test case C a 3D model is preferred.

The analytical solution of the plume height (2.19) is also plotted in Figure 3.1, 3.2 and 3.3 as a red line. The analytical solution follows the numerical interface to some extend. At the time step plotted in Figure 3.1, 3.2 and 3.3 the analytical and numerical solutions are inseparable for $r > 1000$, while for $r < 1000$ there is an discrepancy. Particularly calculates the analytical and numerical solution differently the radius R_H, i.e. the radius at which the CO_2 plume stops filling the aquifer at full height H.

In [24] the analytical solution (2.19) was compared to simulations from a numerical simulator ECLIPSE (Schlumberger Information Systems) for a wide range of subsurface conditions and characteristics of sedimentary basins expected to apply to possible CO_2 injection scenarios. The scenario parameters considered in the article is comparable with the parameters of the test cases considered here, with a cubic k_r-

Model type	3D	VE
Simulation time test case A [s]	450	29
Simulation time test case B [s]	619	25
Simulation time test case B [s]	790	28

Table 3.3: Simulation time of different model types for the test case A,B and C.

s relationship as in test case C. The article concluded that the two-fluid flow dynamics associated with CO_2 injection into deep saline aquifers may be captured very well by the analytical solution (2.19). The conclusions was found to be true for a wide-range of conditions, from warm, very deep formations to shallower, cold formations. The offset in numerical and analytical R_H can however also been seen in this article. The offset is thereby no further examined in this thesis, but left noted as a possible subject for further research.

It is also worth mentioning that the analytical solution is in fact equal in all test cases and assumes instantaneous phase segregation (i.e. zero brine drainage time). Therefore it is not realistic to expect that the analytical and numerical solution are close to identical for all three test cases, as the numerical solutions in the test cases vary greatly.

3.2 Determination of near-well Area

Here, results from determining near-well areas with significant vertical flow is given. Numerical and analytical results are presented separately, before they are compared and discussed. The analysis is restricted to only considering test case C, as VE and 3D simulations were significantly different for this test case.

3.2.1 Numerical Approach

In Figure 3.5 CO_2 saturation, mean vertical CO_2 flux $f_\perp$ and mean horizontal brine flux $f_\parallel$ is plotted after 8 years of injection. Two important observations are made from this figure.

Firstly, the mean vertical flux of brine is largest in the thin, front part of the plume. Here the mean horizontal flux is also at it lowest, which gives that the highest ratio numbers η is located at the front of the plume. In practice this gives that the numerical separation follows the front of the plume. The high values of brine flux results from the horizontal extension of the CO_2 plume, which displaces grid cells initially filled with brine. The plume is here relatively thin compared to other parts of the plume, and it is therefore expected that the brine and CO_2 segregation will occur faster here than in thicker parts of the plume. In the following the flux ratio is therefore not computed numerically for plume heights below some cut off value h_{cut}.

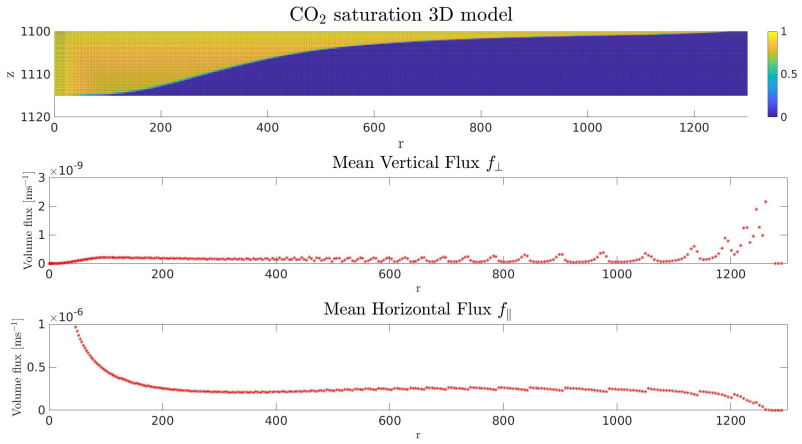

Figure 3.5: CO_2 saturation, mean vertical flux and mean horizontal flux after 8 years of injection in test case C with sharp interface.

The second observation is that both $f_\perp$ and $f_\parallel$ oscillates. As the well is injecting CO_2 at a constant rate, it is not expected to see any oscillatory behaviour in the system and this is thereby assumed to be a non-physical behaviour. The oscillations occur for each stair step of the plume. Here, stair step refers here to a segment of the plume where the bottom cell of the plume is at the same depth. Due to the shape of the plume the stair steps are widest at the front of the plume, and it is also here the oscillations are clearest. The oscillations are expected to be an artefact of the numerical solver and related to the sharp interface assumption and the choice of grid resolution. In Figure 3.6 CO_2 saturation, $f_\perp$ and $f_\parallel$ is plotted at the same time step with the same parameters and grid resolution as in Figure 3.5, except that the sharp interface assumption is removed and the capillary pressure is given as

$$p_{cap}(s_w) = 10\sqrt{\frac{1-s_{r,w}}{s_w - s_{r,w}}} \text{ kPa}$$

The first thing to note in this figure is that the shape of the CO_2 plume in this case is quite different from the case with sharp interface. Further, the oscillations in $f_\perp$ and $f_\parallel$ seen in the simulations with sharp interface are vanished.

The oscillations are also an artefact of the grid resolution. In detail, the oscillations are related to the ratio between the number of grid cells

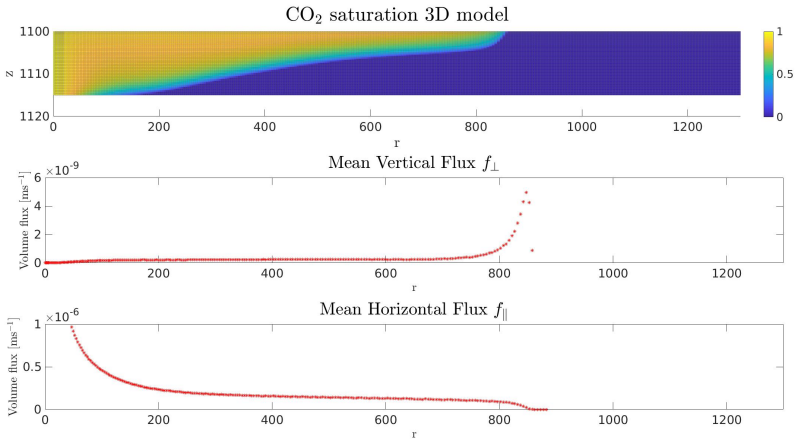

Figure 3.6: CO_2 saturation, mean vertical flux and mean horizontal flux after 8 years of injection in test case C with capillary pressure.

in the vertical (n_z) and radial direction (n_r). It is natural to expect that a higher number of grid cells would increase the precision of a simulation, but a higher number of radial grid cells increases the number of columns in each stair step of the plume. This again increases the oscillatory behaviour. However, an increased number of cells in the vertical direction leads to a smoother shape of the brine-CO_2 interface and a reduction of columns in each stair step of the plume. Therefore, to avoid oscillations there has to be a consistency between the grid resolution in the vertical and radial direction; a fine discretiztion in the radial direction requires a very fine discretization in the vertical direction, which may be computationally demanding. This also exemplifies what was mentioned in the introductory chapter; namely that the grid discretization in the vertical direction in a 3D simulation has to be very fine in order to capture all effects of the system.

In Figure 3.7 $f_\perp$ and $f_\parallel$ are plotted for $h_{cut} = 0.75$m, $n_r = 250$ and $n_z = 250$, which is distinctly different from the original Figure 3.5, where there was no cut-off height and the grid resolution was set by $n_r = 500$ and $n_z = 50$. Here, some oscillations that will affect the flux ratio η are still seen in the plot of the mean vertical flux. Therefore, the ratios presented in the succeeding have been smoothed out using the moving average filtering method, which smooths out each ratio η by replacing it with the average of neighbouring ratios defined within a span. For all results presented in

this thesis this span was set to 5.

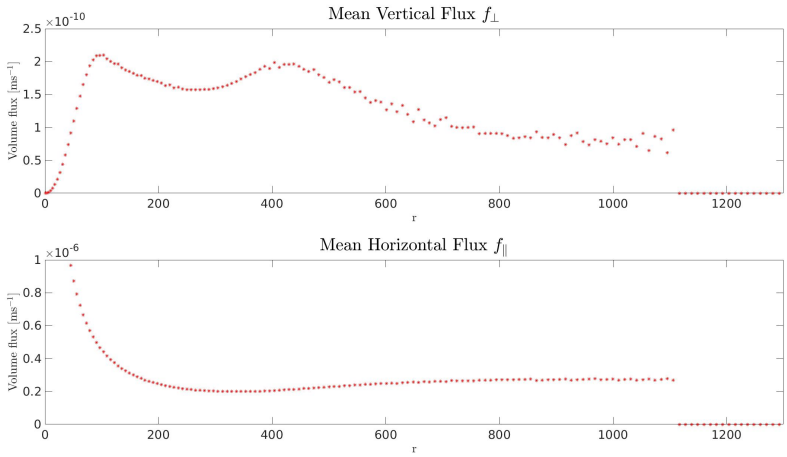

Figure 3.7: Mean vertical and mean horizontal flux with cutoff height $h_{cut} = 0.75$m.

As a result of the discussion above, the remaining results in this section are found by carefully choosing the grid resolution, introducing the cut off value h_{cut} and smoothing out the flux ratio. For $h_{cut} = 0.75$m, $n_r = 250$ and $n_z = 250$ CO_2 saturation and flux ratio is given in Figure 3.8 after 15 years injection. Finally, a plot of the numerical separation radius is given in Figure 3.9 and in Figure 3.10 a contour plot shows the time development of η for the values of h_{cut}, n_r and n_x as given above.

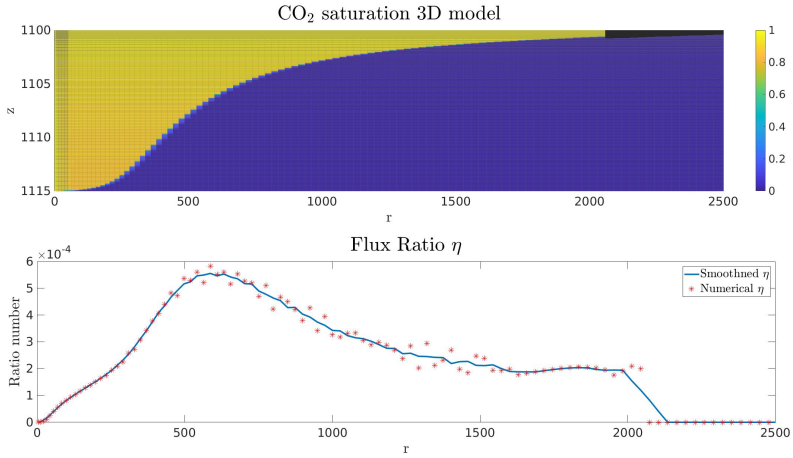

Figure 3.8: CO_2 saturation and flux ratio number η after 15 years of injection. The black cells in the top plot show cells that have been cut out the calculation of η, and the flux ratio is hence zero here as seen in the bottom plot. The red stars in the bottom plot show numerical values of the ratio, and the blue line is the smoothing of these values.

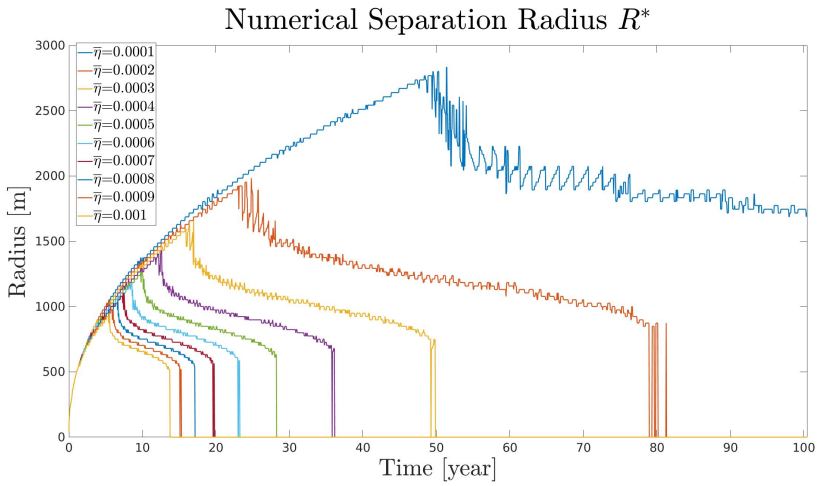

Figure 3.9: Numerically computed separation radii for a range of of threshold values $\overline{\eta}$.

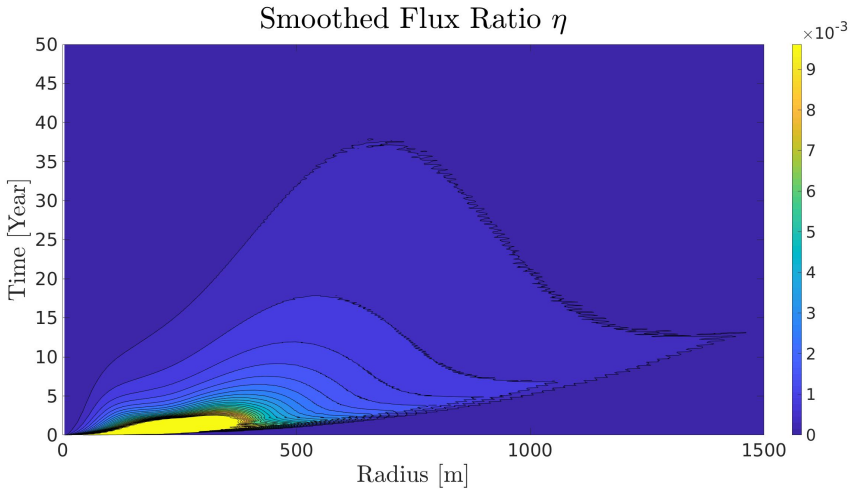

Figure 3.10: Contour plot of numerical flux ratio η.

3.2.2 Analytical Approach

The analytically computed separation radius for a range of $\overline{\eta}$ is presented in Figure 3.11.

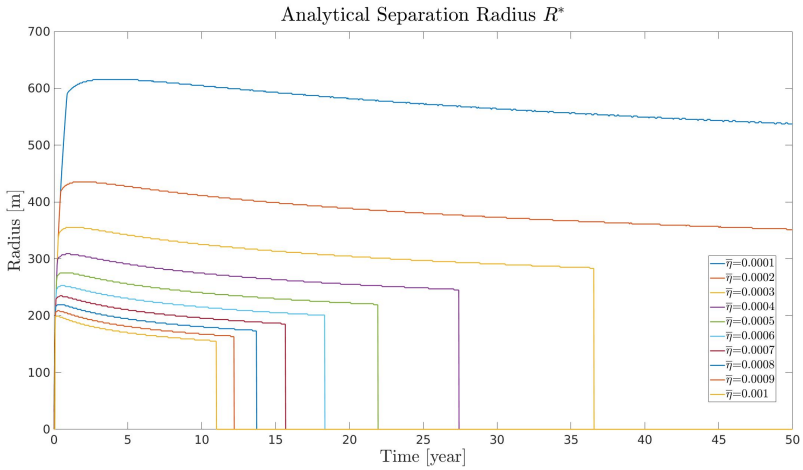

Figure 3.11: Analytical separation radii for a range of of threshold values $\overline{\eta}$.

3.2.3 Comparison and Discussion

Both numerical and analytical separation radius functions are plotted in Figure 3.12. There are both some similarities and clear differences between the analytical and numerical results. Firstly, the numerical and analytical radius are almost identical and increases quickly at the very injection start. However, the analytical radius quickly goes over to lie at almost a constant radius, while the numerical radius continues to rise before it starts to fall at a certain time. At this time the numerical radius reaches it maximal value, and some time later the radius suddenly drops to zero. The analytical radius also drops to zero, but at an earlier time than the numerical radius.

The sudden drops are interpreted as that the brine and CO_2 phases are in vertical equilibrium in the whole aquifer, and that full VE simulations can be conducted after this drop time. The drops may seem non-physical, but can be understood and explained by looking at Figure 3.13. Here the CO_2 plume and the numerical flux ratio η is plotted after 6, 10

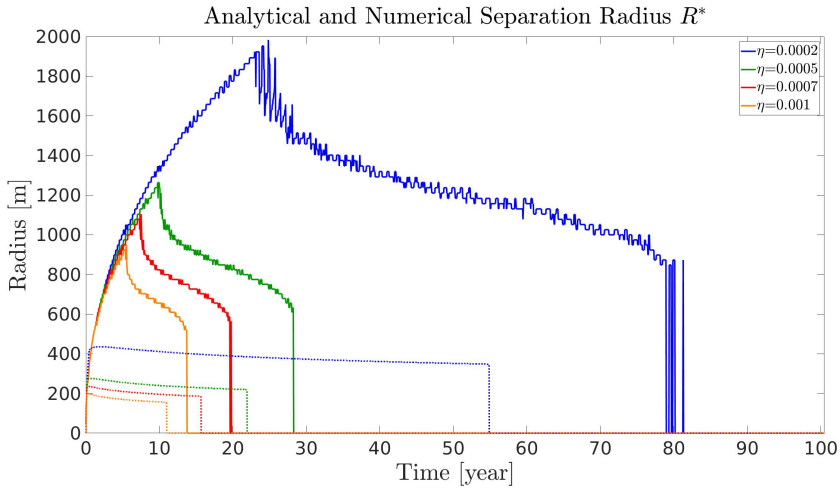

Figure 3.12: Analytical and numerical separation radii for a range of of threshold values $\overline{\eta}$. The analytical and numerical radius is plotted in dotted and solid lines, respectively. The functions with the same colour is found using the same value of $\overline{\eta}$.

and 40 years of injection. This figure illustrates that the maximum value of η approximately lies where the plume height is equal half of the aquifer height H. The maximum value decreases with increasing injection time and at a certain time step the maximum value of η goes below $\overline{\eta}$, giving that VE is assumed in the whole system after this time step.

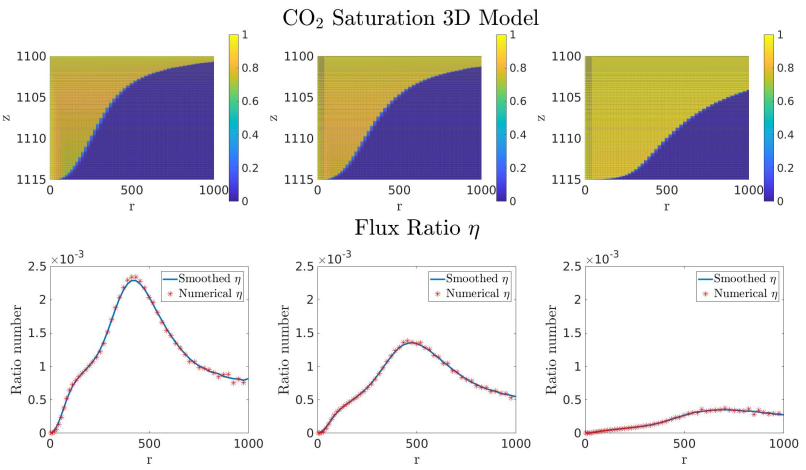

Figure 3.13: CO_2 saturation and flux ratio number η after 6, 10 and 40 years of injection (from left to right).

Furthermore, as there is a great disparity between the analytical and numerical results, it is necessary to examine where the differences come from as the numerical and analytical approach are similar. Particularly the analytical approach aimed to overestimate the separation radius, while results show that the opposite occurs. In particular it is here discussed how similar the numerical and analytical approach are, and if any too bold assumptions have been made in the analytical approach.

In Figure 3.14 and 3.15 the numerical and analytical mean horizontal flux of CO_2 is plotted after 10 and 50 years of injection, respectively. Note that in these figures the cut-off height is set to zero, i.e. the flux is calculated for the whole plume. The analytical and numerical results are equal for $r < R_H$, which was named region I in Section 2.3.2. For $r > R_H$, i.e. in region II, the analytical flux is constant as given in equation (2.20). This to a certain extent consistent with the numerical flux, but the numerical flux lies significantly below the analytical value and also goes to zero at the thin, front part of the plume. Thus, the analytical flux does not capture the physical behaviour of the flux in region II. It is worth to mention that the analytical and numerical flux are more similar after 50 years of injection, see Figure 3.15.

It is not clear exactly which assumptions that lead to the constant analytical flux for in region II. The analytical approach assumes that the CO_2 saturation above the interface $h(r,t)$ is equal to 1, while in reality the

CO_2 plume also consists of some brine. This is especially true for test case C, as brine drainage time in this case is significant. This is also the case that simulations where conducted on in this section. It is not obvious if this assumption leads to the disparity in the horizontal flux, but this is left as a possible cause and pointed out as further research.

The practical impact of the assumed too high analytical horizontal flux of CO_2 is that the analytical approach assumes a too high maximum vertical flux, $f_{\perp}^{max}$. Thus vertical equilibrium may be assumed easier in the analytical approach giving lower values of the separation radius compared to the numerical radius as seen in Figure 3.12.

The practical impact becomes very clear by examining Figure 3.16 and 3.17. In these figures the area where vertical equilibrium is assumed is plotted as green in the (r,t)-plane. In the figures the radii R_H and R_F are also plotted, such that between these two lines the CO_2 plume goes from filling the aquifer at full height H to height zero. This is what was referred to as region II in Section 2.3.2. In this region the difference in the results between the numerical and analytical approach are clearest. The analytical approach assumes the VE assumption to hold almost everywhere between these two radii, while this is definitely not the case in the numerical approach. In region II the analytical horizontal flux is constant, while region I the analytical and numerical flux are almost identical. In region I the analytical approach is more strict to assume VE compared the numerical approach, as was aimed for. Thus is seems clear that the inconsistency is related to the horizontal fluxes, while it is not trivial to explain the exact cause of the inconsistency.

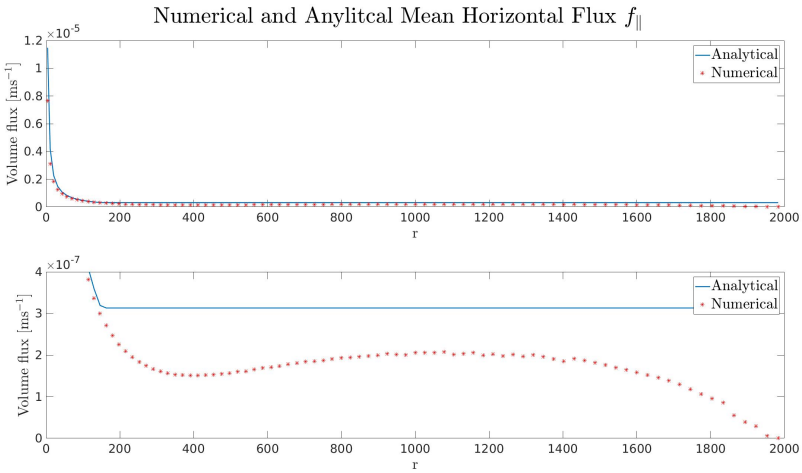

Figure 3.14: Plot of numerical and analytical mean horizontal flux of CO_2 after 10 years of injection. The difference between the top and bottom plot is the range and scaling of the y-axis.

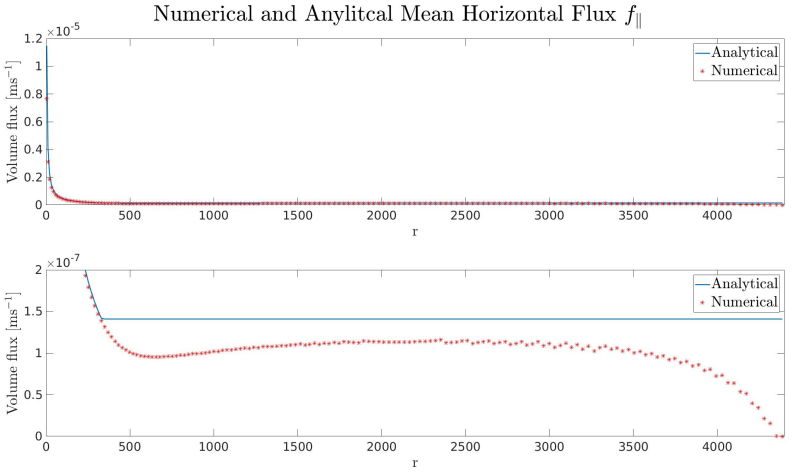

Figure 3.15: Plot of numerical and analytical horizontal flux after 50 years of injection. The difference between the top and bottom plot is the range and scaling of the y-axis.

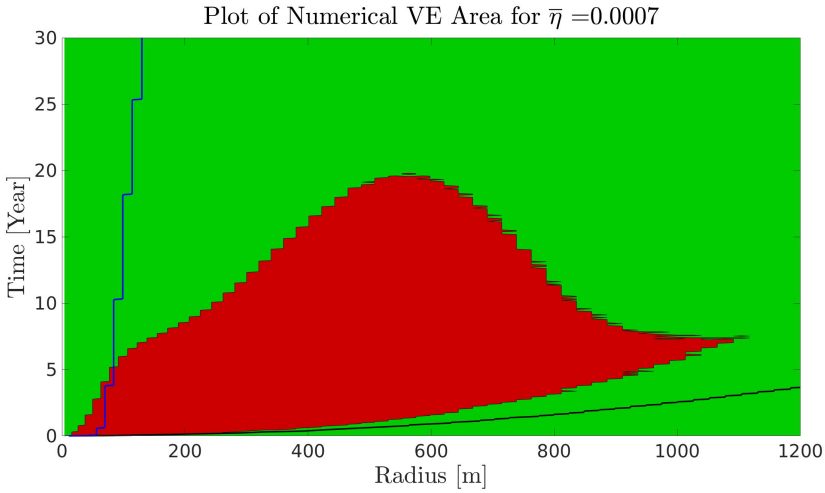

Figure 3.16: Plot of areas where the vertical equilibrium is assumed to hold (green) and not (red) for threshold value $\overline{\eta} = 0.0007$ with numerical approach. The blue and black lines indicates where the position of the numerically determined radii $R_H(t)$ and $R_F(t)$.

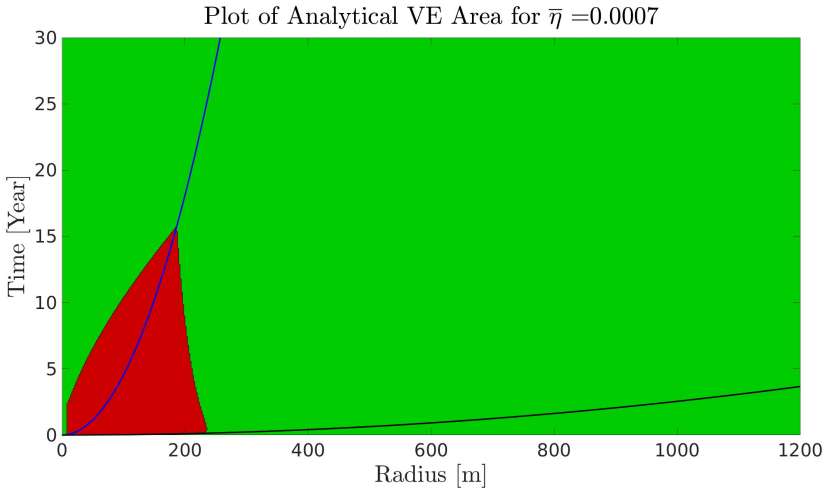

Figure 3.17: Plot of areas where the vertical equilibrium is assumed to hold (green) and not (red) for threshold value $\overline{\eta} = 0.0007$ with analytical approach. The blue and black lines indicates where the position of the analytical radii $R_H(t)$ and $R_F(t)$.

Further, the analytical approach aimed to rather overestimate than underestimate the separation radius by assuming that the drainage of brine at a radius r is initiated when the CO_2 plume first reaches r and using the maximum value of $f_\perp$ in order for the VE assumption to hold. The first assumption was implemented by including the front time t_F, and should clearly contribute to some overestimation in the analytical separation radius. However, it is discussable if the second assumption contributes to an overestimation. If a column is considered to be in vertical equilibrium according to some value of $\overline{\eta}$, then per definition is $\frac{f_\perp}{f_\parallel} \leq \overline{\eta}$. Assume for now that the analytical approach used the value $f_\perp^{mid} = \frac{1}{2}\overline{\eta} f_\parallel$ instead of $f_\perp^{max}$ to find the segregation time t^*. As $f_\perp^{mid} < f_\perp^{max}$ this is equivlant to a smaller vertical flux of brine, and this is related to a *higher* segregation time t^*. This agian, yields that using $f_\perp^{mid}$ instead of $f_\perp^{max}$ the VE assumption still holds, but results in a larger separation radius. Therefore it is first of all questionable if using the value $f_\perp^{max}$ gives a valid representation of the segregation time, and secondly if it contributes to an overestimation of the separation radius.

Another element of uncertainty is if the characteristic speed v^* captures the time behaviour of the brine drainage, as the original one dimensional mass conservation equation (2.21) was simplified under two assumptions. Firstly, the capillary pressure was assumed to be zero which is in full consistency with the numerical simulations. Secondly, is was assumed that the total vertical volume flux $v = v_w + v_n$ was negligible. This lead to an expression of the vertical flux of brine that only was dependent on brine saturation, as well as the scalar hyperbolic conservation law for mass conservation (2.24). As vertical drainage of brine is being modelled, it might be a peculiar and bold assumption to assume that the total vertical volume flux is negligible. To verify if this a valid assumption, numerical simulations of brine drainage in single columns can be made to see if they are consistent with analytical results. However, the analytical approach assumes that the brine saturation is equal s_w^* at the top of the plume, which in fact leads to an overestimation of the separation radius, and that the brine saturation is less than 0.5 within the CO_2 plume, but there are no assumptions or information of *exactly* how the brine profile is downwards in the plume. In order to perform numerical simulations, the saturation profile is needed as an initial condition. Therefore some assumption of the profile has to be made, and this thesis will not go into further details here but leave this as a possible task for further research.

To summarize, the analytical and numerical separation radius are

comparable to a certain extend, but there are some major differences. Especially the analytical approach aimed for overestimating the separation radius, while the results show that it in fact underestimates the radius. It is argued for that this probably is due to a poor consistency between the analytical and numerical mean horizontal flux of CO_2, $f_{\parallel}$, but there are also uncertainties related to other elements in the analytical approach. The hope was that the analytical approach could be used as an estimation for the separation radius, but from the results and discussion presented in this section it is clear that some further examinations and improvements have to be done before the analytical results can be applied.

3.3 Hybrid Model

The separation radius function $R^*(t)$ determines the performance of a hybrid model. Here numerical results from simulations with three different separation radius functions are presented and compared to pure VE and 3D simulations. The separation functions can be seen in Figure 3.18, and as seen here the three functions and thereby their related hybrid model is hereafter referred to as the constant, linear and stair step separation function and model. Inspired by the results in Section 3.2 about determination of the near-well area, the linear and stair step function goes to a small value at a certain time step. The scenario parameters are as described in Tabular 3.1 and 3.2 as test case C.

3.3.1 Numerical Results

Figure 3.20 shows CO_2 saturation after 20 years of injection for the different model types and Figure 3.21 shows the difference of the VE model and hybrid models compared to the 3D model. In Figure 3.19 the mean cell saturation differences for the VE model and hybrid models compared to the 3D model are plotted. Tabular 3.4 presents simulation times of the different models.

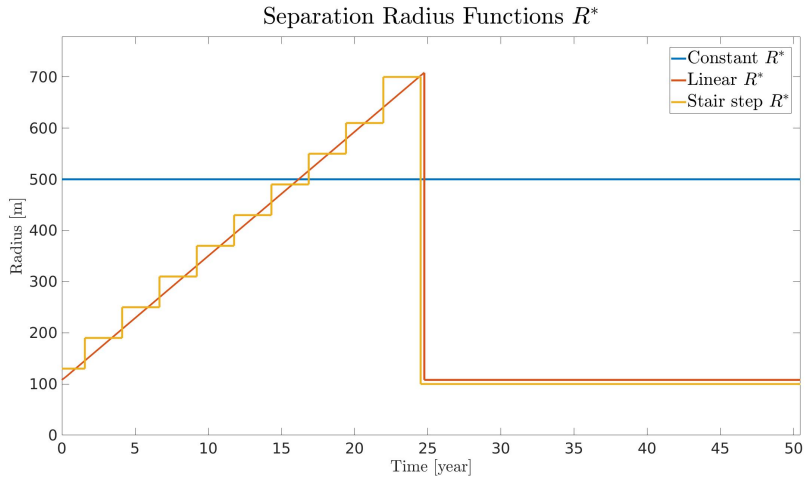

Figure 3.18: Different separation function $R^*(t)$.

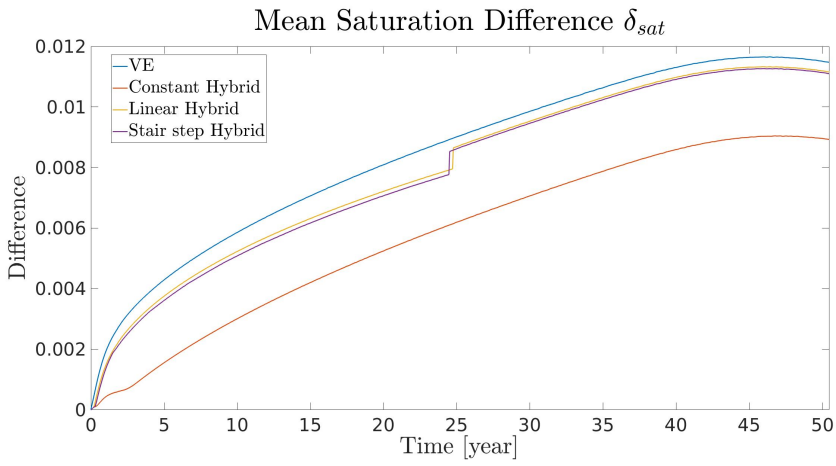

Figure 3.19: Mean saturation difference for a VE simulation and hybrid simulations with the constant, linear and stair step separation radius functions compared to a 3D simulation.

Model type	3D	VE	Constant hybrid	Linear hybrid	Stair step hybrid
Simulation time [s]	225	48	111	436	97
Percentage of 3D simulation	-	21 %	49 %	194 %	43 %
Conversion time [s]	-	-	1,7	309	7,5
Percentage conversion time	-	-	1,5 %	71 %	7,7 %

Table 3.4: Simulation time of different hybrid models. Conversion time refers here to the simulation time used to redefining hybrid models as the separation radius (and hence the VE and 3D domain) changes.

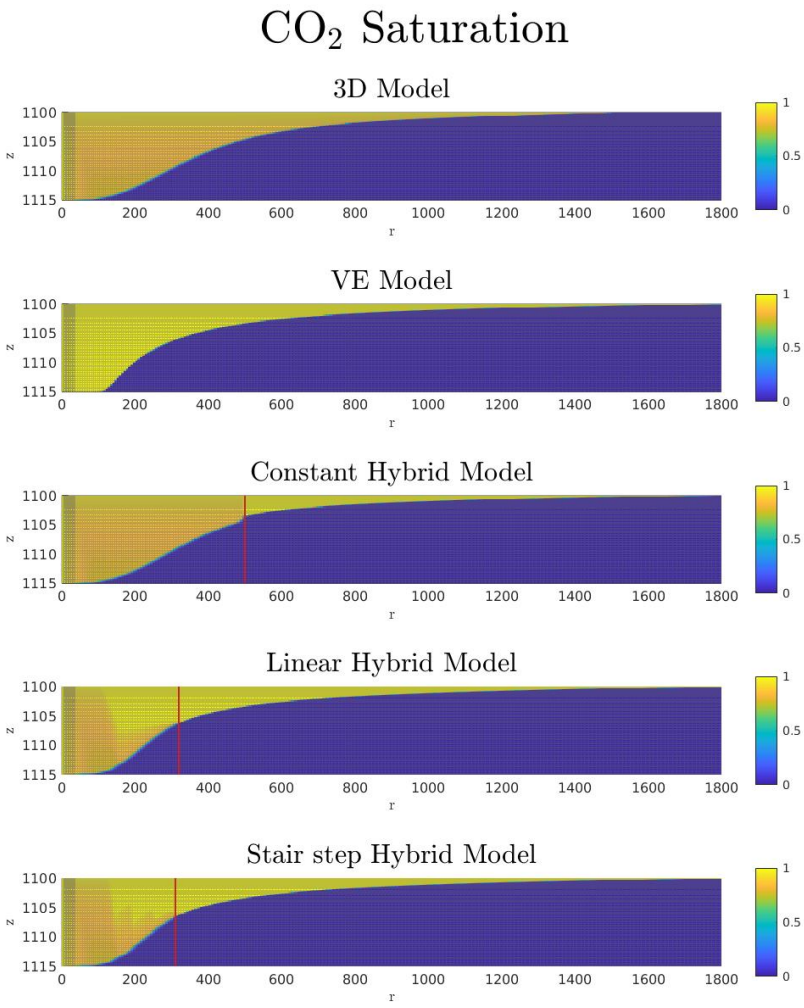

Figure 3.20: CO_2 saturation after 9 years of injection for different model types. The red line in plots for the hybrid models defines the interface between the 3D and VE domain, i.e. in the simulations the area to the left of the line is the 3D domain and the area to the right is the VE domain.

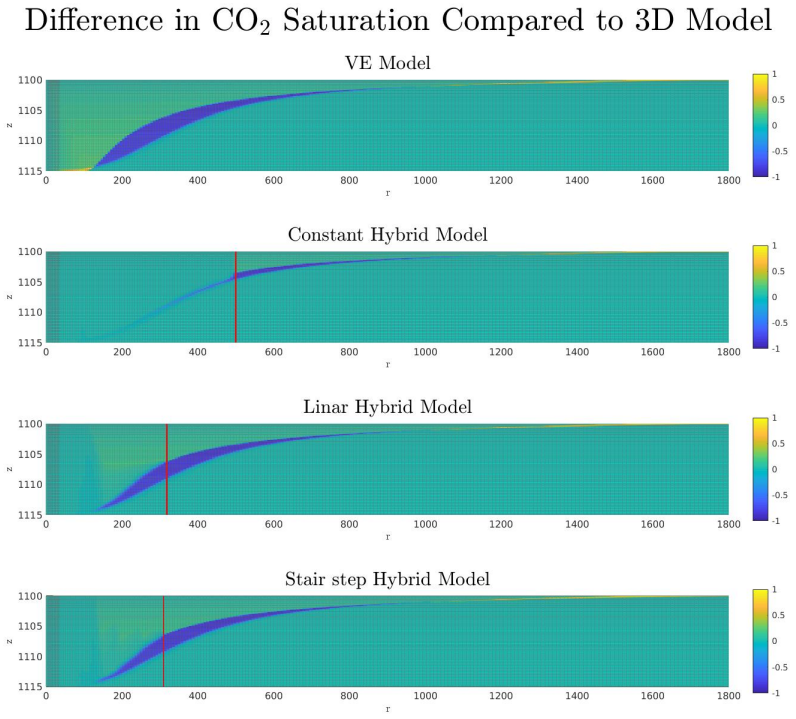

Figure 3.21: Difference in CO_2 saturation after 9 years of injection for different model types. The red line in plots for the hybrid models defines the interface between the 3D and VE domain, i.e. in the simulations the area to the left of the line is the 3D domain and the area to the right is the VE domain.

3.3.2 Discussion

As presented in Figure 3.20 and 3.21 the hybrid models are more accurate than the VE model. In fact it is clear that the accuracy of the hybrid models are determined by the size of the 3D domain. As seen in Figure 3.21 the constant hybrid model nearly reproduces the assumed correct 3D solution within the constant radius, only interrupted by some interface boundary effects between the VE and 3D domain. If the constant radius was increased to a higher value, it is expected that the constant hybrid model would be even more accurate, with the cost of increased computational time as the total number of grid cells would increase.

From Figure 3.21 and 3.19 it can be seen that the solution of the linear and stair step hybrid model are quite equal. This is expected, as the linear and stair step separation functions also are quite equal. However, the linear model is more than 4 times slower that the stair step model. In fact, the linear model is also much slower than the full 3D model. This due to how the hybrid model is implemented. The linear separation function is also a stair step function, only that the intervals of this function are so small that they are not visible in Figure 3.18. For the simulation data presented in Tabular 3.4, the linear hybrid model has been redefined 50 times between each time the stair step model is redefined. Therefore, the conversion time in the linear model is very large and stands for 71 % of the total simulation time. This illustrates that a hybrid model can perform very well even though the separation function is not continuous.

The results also show that there is a trade-off between the two interests of a hybrid model; the correctness of the 3D model and the fastness of a VE model. A hybrid model with a large 3D domain is more precise and slower than a hybrid model with a large VE domain. The stair step hybrid model is the fastest of the hybrid models, but is less accurate than the constant hybrid model, which throughout the simulation time has the largest 3D domain.

The overall goal with a hybrid model is to get a model that outperforms both a VE and a 3D model for certain injection scenarios. All hybrid models are both more accurate and slower than than the VE model. The linear hybrid model is as mentioned slower than the pure 3D model, and is thereby no improvement. The simulation time of the constant and stair step model are about half of the simulation time of the 3D model and twice of the simulation of the VE model. One could not expect a hybrid to be as fast as a VE model, but this shows that the accuracy of a

hybrid model can be much greater than the accuracy of a VE model, at some extra computational cost. It is also worth to remark that the simulations here are limited 50 years of injection, while simulations for studying long-term effects of CO_2 storage can be up to thousands of years after injection stop. Both numerical and analytical results from determining the near-well area showed that after some time vertical equilibrium can be assumed in the whole aquifer of the test case. After this time the hybrid model could be equal a full VE model, and for long-time simulations this should minimize the relatively large time difference between hybrid and VE models presented here.

Chapter 4

Conclusion and Further Work

4.1 Conclusion

In this thesis new insight concerning the vertical equilibrium assumption have been presented by numerical simulations and analytical results. Research has earlier been made to illustrate the applicability of VE models [20, 25], but this thesis takes this a step further by *quantifying* where the vertical equilibrium holds by considering the ratio of mean vertical volume flux of brine to mean horizontal volume flux of CO_2. The ratio is determined numerically and also used in an analytical approach to quantify areas where vertical equilibrium can be assumed.

Numerical simulations with `MRST` showed both great consistency and significant disparities between VE and 3D models in the vicinity of an vertically injecting well. The consistency between the models was limited to cases with high vertical drainage of brine within the CO_2 plume, while a case with permeability 10mD and a cubic k_r-s relationships showed great discrepancy. From this it is clear that some caution about rock and fluid properties should be made before the fast VE model is used in short-term simulations.

A numerical and analytical approach was presented and implemented to determine areas where vertical equilibrium can be assumed to hold by calculating a separation radius around an injecting well. The analytical approach aimed to overestimate the numerical separation radius, but results presented showed that the opposite occurs. It is argued for that this probably is due to overestimation of the analytical mean horizontal flux of CO_2, but there are also other elements in the analytical approach that should be examined before any conclusions are made. Furthermore,

both approaches showed that VE could be assumed in the whole aquifer after some time. This indicates that a hybrid models an be transformed to full VE models after a certain time, which suggests that hybrid models can be used for long-term simulations with only limited computational penalty compared to a pure VE model.

Simulations with a hybrid model showed promising results compared to simulations with pure VE and 3D models. The hybrid models were able to obtain the accuracy of full 3D models in the vicinity of an injection well, while still benefiting from the lower computational requirements associated with VE-type modelling farther away from the well. The accuracy near the well is significantly higher than that of a pure VE model, but to a greater computational cost. Thereby, it is reasonable that hybrid models can replace a more computational demanding 3D model in the injection phase, while more simulations have to be made before hybrid models can be compared to full VE models for long-term scenarios.

4.2 Further Work

As pointed out in the discussion parts in Chapter 3, further work of this thesis is mostly related to the analytical approach for determining the separation radius. Especially this is related to see if improvements can be made to determine the mean horizontal volume flux $f_{\parallel}$ and improve consistency between numerical and analytical approach. An important issue is to investigate if using the value $f_{\perp}^{max} = \overline{\eta} f_{\parallel}$ connects the numerical and analytical approach in a appropriate way. It is also pointed out that work can be done to see if the analytical approach represents the brine drainage time correctly by using analysis of characteristics.

The analytical approach was developed with a view to be as similar as possible to the numerical approach. However, there are other ways of determining if the VE assumptions holds analytically. Particularly, what was named the characteristics saturation level s_w^* can be set to a predefined value, instead of calculating it by assuming that $f_{\perp}^{max} = \overline{\eta} f_{\parallel}$. With this approach, the analytical approach omits to use the horizontal flux $f_{\parallel}$. The value of s_w^*, instead of $\overline{\eta}$, then sets the strictness of the vertical equilibrium assumption. A low value of s_w^* corresponds to long brine drainage time and a strict separation radius function. Simulations of hybrid models with separation radius function for a range of s_w^*-values can be conducted to empirically determine which values of s_w^* are able to

determine the near-well area.

Numerical simulations with a 3D model and a sharp interface assumptions showed that both vertical and horizontal fluxes oscillates. This was argued to be a non-physical behaviour and related to the sharp interface assumption, as simulations with a capillary fringe did not prove to have the same oscillatory behaviour. Is is possible that the oscillations come from the numerical method used to solve the implicit equation system (2.8). Thereby work can be done to first and foremost identify the source of the oscillations, and then take actions from this.

Another interesting topic is to study the long-term behaviour of hybrid models, especially where the hybrid model after some time is converted to a pure VE model. It is also worth to note that the hybrid model used here was not optimized for computational efficiency, and can be greatly improved by handling the way one hybrid model is converted into another hybrid model with different VE and 3D domain.

Bibliography

[1] IPCC. *IPCC 2014: Climate Change 2014: Synthesis Report. Contribution of Working Groups I, II and III to the Fifth Assessment Report of the Intergovernmental Panel on Climate Change*. IPCC, Geneva, Switzerland, 151 pp., 2014.

[2] The Paris Agreement. http://unfccc.int/paris_agreement/items/9485.php, 2015. Accessed: 2017-03-27.

[3] Paris Agreement. https://ec.europa.eu/clima/policies/international/negotiations/paris_en, 2015. Accessed: 2017-03-27.

[4] J.M Nordbotten and M. A. Celia. *Goelogical Storage of CO2 - Modeling Approaches for Large-Scale Simulation*. John Wiley & Sons, Incorporated, 1 edition, 2011.

[5] IPCC. *Assessing Transformation Pathways. Climate Change 2014: Mitigation of Climate Change. Contribution of Working Group III to the Fifth Assessment Report of the Intergovernmental Panel on Climate Change*. IPCC, Cambridge University Press, 2014.

[6] IPCC 2015. *IPCC Special Report on Carbon Dioxide Capture and Storage. Prepared by Working Group III of the Intergovernmental Panel on Climate Change [Metz, B., O. Davidson, H. C. de Coninck, M. Loos, and L. A. Meyer (eds.)]*. Cambridge University Press, Cambridge, United Kingdom and New York, NY, USA, 442 pp., 2005.

[7] T Maldal and I.M Tappel. CO2 underground storage for snøhvit gas field development. *Energy*, 29(9-10):1403–1411, jul 2004. doi: 10.1016/j.energy.2004.03.074. URL https://doi.org/10.1016%2Fj.energy.2004.03.074.

[8] *The MATLAB Reservoir Simulation Toolbox, version 2016b, 12 2016*. http://www.sintef.no/mrst/, 2016.

[9] Knut-Andreas Lie. An introduction to reservoir simulation using matlab: User guide for the matlab reservoir simulation toolbox (mrst). *SINTEF ICT, May*, 2014.

[10] SINTEF Digital. *The MATLAB Reservoir Simulation Toolbox: Numerical CO_2 library, versionn 2016b, 12 2016*. http://www.sintef.no/co2lab, 2016.

[11] Odd Andersen. *Simplified models for numerical simulation of geological CO2 storage*. PhD thesis, University of Bergen, 2017.

[12] S. E. Gasda, J. M. Nordbotten, and M. A. Celia. Vertical equilibrium with sub-scale analytical methods for geological co2 sequestration. *Computational Geosciences*, 13(4):469, 2009. ISSN 1573-1499. doi: 10.1007/s10596-009-9138-x. URL http://dx.doi.org/10.1007/s10596-009-9138-x.

[13] Bo Guo, Karl W. Bandilla, Jan M. Nordbotten, Michael A. Celia, Eirik Keilegavlen, and Florian Doster. A multiscale multilayer vertically integrated model with vertical dynamics for co2 sequestration in layered geological formations. *Water Resources Research*, 52 (8):6490–6505, 2016. ISSN 1944-7973. doi: 10.1002/2016WR018714. URL http://dx.doi.org/10.1002/2016WR018714.

[14] Odd Andersen, Knut-Andreas Lie, and Halvor Møll Nilsen. An open-source toolchain for simulation and optimization of aquifer-wide co2 storage. *Energy Procedia*, 86:324 – 333, 2016. ISSN 1876-6102. doi: http://dx.doi.org/10.1016/j.egypro.2016.01.033. URL http://www.sciencedirect.com/science/article/pii/S1876610216000357.

[15] George F. Pinder and Michael A. Celia. *Subsurface Hydrology*. Wiley-Blackwell, sep 2006. doi: 10.1002/0470044209. URL https://doi.org/10.1002%2F0470044209.

[16] J. M. Nordbotten and H. K. Dahle. Impact of the capillary fringe in vertically integrated models for co2 storage. *Water Resources Research*, 47(2):n/a–n/a, 2011. ISSN 1944-7973.

doi: 10.1029/2009WR008958. URL http://dx.doi.org/10.1029/2009WR008958. W02537.

[17] Jonathan P Ennis-King, Lincoln Paterson, et al. Role of convective mixing in the long-term storage of carbon dioxide in deep saline formations. *Spe Journal*, 10(03):349–356, 2005.

[18] O. Andersen, S. E. Gasda, and H. M. Nilsen. Vertically averaged equations with variable density for co_2 flow in porous media. *Transport in Porous Media*, 107(1):95–127, 2015. ISSN 1573-1634. doi: 10.1007/s11242-014-0427-z. URL http://dx.doi.org/10.1007/s11242-014-0427-z.

[19] S Benson, R Pini, C Reynolds, and S Krevor. Relative permeability analysis to describe multi-phase flow in co2 storage reservoirs. *Global CCS Institute*, 2013.

[20] Benjamin Court, Karl W. Bandilla, Michael A. Celia, Adam Janzen, Mark Dobossy, and Jan M. Nordbotten. Applicability of vertical-equilibrium and sharp-interface assumptions in {CO2} sequestration modeling. *International Journal of Greenhouse Gas Control*, 10:134 – 147, 2012. ISSN 1750-5836. doi: http://doi.org/10.1016/j.ijggc.2012.04.015. URL http://www.sciencedirect.com/science/article/pii/S1750583612001041.

[21] JAN M. NORDBOTTEN and MICHAEL A. CELIA. Similarity solutions for fluid injection into confined aquifers. *Journal of Fluid Mechanics*, 561:307–327, 2006. doi: 10.1017/S0022112006000802.

[22] I. Aavatsmark. Bevarelsesmetoder for hyberbolske differensialligninger. Technical report, Institutt for Informatikk, University of Bergen, 2004.

[23] Helge Holden and Nils Henrik Risebro. *Front tracking for hyperbolic conservation laws*, volume 152. Springer, 2015.

[24] Jan Martin Nordbotten, Michael A. Celia, and Stefan Bachu. Injection and storage of co2 in deep saline aquifers: Analytical solution for co2 plume evolution during injection. *Transport in Porous Media*, 58(3):339–360, 2005. ISSN 1573-1634. doi: 10.1007/s11242-004-0670-9. URL http://dx.doi.org/10.1007/s11242-004-0670-9.

[25] Bo Guo, Karl W. Bandilla, Eirik Keilegavlen, Florian Doster, and Michael A. Celia. Application of vertically-integrated models with subscale vertical dynamics to field sites for co2 sequestration. *Energy Procedia*, 63:3523 – 3531, 2014. ISSN 1876-6102. doi: http://dx.doi.org/10.1016/j.egypro.2014.11.381. URL http://www.sciencedirect.com/science/article/pii/S1876610214021961.

Appendix A

Nomenclature

A.1 Abbreviations

Symbol	Description
nw	Non-wetting
w	Wetting
res	Residual
cap	Capillary
VE	Vertical equilibrium
CCS	Carbon capture and storage
IPCC	The Intergovernmental Panel on Climate Changes
MRST	MATLAB Reservoir Simulation Toolbox

A.2 Arabic Letters

Symbol	Description
A	Areal
c	Compressibility
f	Fine-scale mass flux
$\mathbf{F}$	Mass flux
$f_{\perp}$	Mean vertical volume flux
$f_{\parallel}$	Mean horizontal volume flux
$\mathscr{F}$	Faces of a cell
$\boldsymbol{g}$	Gravitational vector
g	Flux function
g'	Characteristic speed
h	Height of CO_2 plume
H	Height of aquifer
k_r	Relative permeability
$\boldsymbol{K}$	Permeability tensor
k	Absolute permeability
n	Number of grid cells in a direction
p	Fine-scale pressure
P	Coarse-scale pressure
p_{cap}	Capillary pressure
Q	Injection rate
R^*	Separation radius
R_H	Radius
R_F	Radius
s	Fine-scale saturation
S	Coarse-scale saturation
s_w^*	Characteristic saturation level
t^*	Segregation time
t_f	Front time
$\boldsymbol{u}$	Fine-scale volumetric flux
u	Density
$\boldsymbol{v}$	Fine-scale fluid velocity
v^*	Characteristic speed
V	Set of cells

A.3 Greek Letters

Symbol	Description
α	Phase index
β	Dimensionless parameter
γ	Specific weight
Γ	Interface
δ	Mean saturation difference
ζ	Aquifer surface
η	Mass flux ratio number
$\bar{\eta}$	Vertically averaged mass flux ratio
θ	Aquifer slope
Θ	Slice angle
$\boldsymbol{\kappa}$	Coarse-scale permeability
λ	Mobility ratio
λ	Fine-scale mobility
Λ	Coarse-scale mobility
ρ	Mass density
ϕ	Fine-scale porosity
Φ	Coarse-scale porosity
Θ	Coupled porosity
μ	Viscosity
ν	Volumetric flux
χ	Dimensionless parameter
ψ	Fine-scale mass source density
Ψ	Coarse-scale mass source density
Ξ	Coupled mass source density
Υ	Coupled saturation
Π	Coupled Pressure
ω	Slice angle
Ω	Domain
$\partial\Omega$	Boundary of domain